

Tracking hidden magnetospheric fluctuations in accretion-powered pulsars with a Kalman filter

A. Melatos^{1,2} and N. J. O’Neill^{1,2} and P. M. Meyers^{1,2,3} and J. O’Leary^{1,2}

amelatos@unimelb.edu.au

ABSTRACT

X-ray flux and pulse period fluctuations in an accretion-powered pulsar convey important information about the disk-magnetosphere interaction. It is shown that simultaneous flux and period measurements can be analysed with a Kalman filter based on the standard magnetocentrifugal accretion torque to generate accurate time-dependent estimates of three hidden state variables, which fluctuate stochastically and cannot be measured directly: the mass accretion rate, the Maxwell stress at the disk-magnetosphere boundary, and the radiative efficiency of accretion onto the stellar surface. The inferred fluctuation statistics carry implications for the physics of hydromagnetic instabilities at the disk-magnetosphere boundary and searches for continuous gravitational radiation from low-mass X-ray binaries.

Subject headings: pulsars: general — stars: neutron — stars: rotation

1. Introduction

Coherent X-ray timing of accretion-powered pulsars affords insights into how the angular velocity $\Omega(t)$ of the neutron star and its time derivative $\dot{\Omega}(t)$ fluctuate stochastically in response to the hydromagnetic accretion torque. Timing data from satellite missions such as the *Compton Gamma Ray Observatory*, *Rossi X-Ray Timing Explorer (RXTE)*, and *Neutron Star Interior Composition Explorer (NICER)* (Gendreau et al. 2016) reveal a number of intriguing, torque-related phenomena, including torque reversals, pulse profile phase delays

¹School of Physics, University of Melbourne, Parkville, VIC 3010, Australia

²Australian Research Council Centre of Excellence for Gravitational Wave Discovery (OzGrav), Parkville, VIC 3010, Australia

³Theoretical Astrophysics Group, California Institute of Technology, Pasadena, CA 91125, USA

at the fundamental frequency and its harmonics, phase-flux correlations, and red noise in the power spectral density (PSD) of $\Omega(t)$ and $\dot{\Omega}(t)$ (Bildsten et al. 1997; Riggio et al. 2008; Yang et al. 2017; Patruno & Watts 2021; Serim et al. 2021). Simultaneously, high-time-resolution measurements of fluctuations in the aperiodic X-ray luminosity $L(t)$ shed light on the physics of the accretion disk and disk-magnetosphere boundary. Observed phenomena include nonstationarity, red noise in the PSD of $L(t)$ (typically a doubly broken power-law), quasiperiodic oscillations whose frequencies depend on flux, and a linear scaling between flux and root-mean-square variability, which extends to other accreting compact objects such as active galaxies (Uttley & McHardy 2001; Revnivtsev & Mereghetti 2015; Patruno & Watts 2021; De Marco et al. 2022).

In principle, $\Omega(t)$ and $L(t)$ fluctuations can be related theoretically, as both variables depend on the mass accretion rate under the canonical magnetocentrifugal hypothesis (Ghosh & Lamb 1979). Magnetocentrifugal accretion is consistent with phenomenological properties of accretion-powered pulsars at the population level and in individual objects, e.g. the recycling scenario confirmed by the discovery of SAX J1808.4–3658, and the spin-up line for radio millisecond pulsars in the Ω – $\dot{\Omega}$ plane (Patruno & Watts 2021). However the disk-magnetosphere interaction is complicated geometrically and hydromagnetically; three-dimensional simulations predict the emergence of twisted magnetic field structures disrupted episodically by instabilities at the disk-magnetosphere boundary (Romanova et al. 2003, 2005; Kulkarni & Romanova 2008). Consequently it is challenging to reconcile the measured time series $\Omega(t)$ and $L(t)$ in detail in individual objects, predict correlations like $\langle \Omega(t)L(t') \rangle$, and predict the origin and onset of phenomena such as quasiperiodic oscillations. Progress has occurred in certain directions, e.g. employing autoregressive moving average models to study torque-luminosity correlations of the form $\langle \dot{\Omega}(t)L(t') \rangle$ (Baykal & Oegelman 1993), and testing for consistency with random walk and shot noise processes (de Kool & Anzer 1993; Baykal 1997; Lazzati & Stella 1997). Evidence has also been reported for a break in the power-law PSD of $L(t)$ near the neutron star spin frequency (and hence the Kepler frequency at the disk-magnetosphere boundary) for accretion-powered X-ray pulsars near magnetocentrifugal equilibrium (Revnivtsev et al. 2009; Revnivtsev & Mereghetti 2015; Mönkkönen et al. 2022). Torque-luminosity modeling has been performed on GRO J1744–28 and 2S 1417–624, using a phenomenological torque-luminosity scaling of power-law form (Sanna et al. 2017; Serim et al. 2021).

Understanding the time-dependent connection between $\Omega(t)$ and $L(t)$ has become an imperative recently in another field: gravitational wave astronomy. Searches for continuous, quasimonochromatic, gravitational wave signals from accretion-powered pulsars are a priority for long-baseline detectors such as the Laser Interferometer Gravitational Wave Observatory (LIGO) (Middleton et al. 2020; The LIGO Scientific Collaboration, et al. 2021).

The target list extends beyond accretion-powered pulsars to embrace nonpulsating accreting neutron stars in low-mass X-ray binaries, including sources that exhibit thermonuclear burst oscillations and kilohertz quasiperiodic oscillations, where $\Omega(t)$ is measured intermittently or not at all (Watts et al. 2008; Riles 2013, 2022). The PSD of $\Omega(t)$ affects the gravitational wave sensitivity, because it limits the coherence time T_{drift} of a search with an optimal matched filter, which assumes that $\Omega(t)$ evolves deterministically (Watts et al. 2008; Riles 2013; Mukherjee et al. 2018; Riles 2022). Semicohherent algorithms have been developed to track stochastic fluctuations in $\Omega(t)$ (Goetz & Riles 2011; Whelan et al. 2015; Suvorova et al. 2017; Melatos et al. 2021) but they require T_{drift} to be known in advance. In nonpulsating systems, where $\Omega(t)$ cannot be measured directly, it would be advantageous to infer T_{drift} from luminosity fluctuations, i.e. from the observed PSD of $L(t)$. A pioneering study with this goal was completed by Mukherjee et al. (2018), but work remains to be done. A general theoretical understanding of the connection between $\Omega(t)$ and $L(t)$ would prove valuable in this context.

In this paper, we demonstrate a new, self-consistent, signal processing framework based on a Kalman filter to relate simultaneous observations of the time series $\Omega(t)$ and $L(t)$ to the canonical dynamical model of magnetocentrifugal accretion and track the evolution of hidden state variables of physical interest, such as the Maxwell stress at the disk-magnetosphere boundary. The Kalman filter framework extends previous studies in three ways. (i) It connects $\Omega(t)$ and $L(t)$ through a specific physical model of accretion, namely the magnetocentrifugal model, instead of invoking a generic random process (e.g. shot noise) or a phenomenological torque-luminosity scaling (e.g. power law). (ii) It tracks the progress of the system through the most likely sequence of hidden states consistent with the specific time-ordered $\Omega(t)$ and $L(t)$ data observed, instead of ensemble-averaged statistics such as the associated PSDs. (iii) It infers the statistics of $\Omega(t)$, $L(t)$, and the hidden state variables simultaneously, rather than constructing PSDs for $\Omega(t)$ and $L(t)$ before relating them to the underlying accretion dynamics. The paper shares some features with recent work to estimate, using a Kalman filter, the parameters of the classic, two-component, crust-superfluid model of a neutron star driven by timing noise (Baykal et al. 1991; Meyers et al. 2021), although the latter reference does not analyse $L(t)$; see also Meyers et al. (2021). The paper also shares some features with recent work applying continuous-time autoregressive moving average (CARMA) models and their variants to a diverse selection of astrophysical massive time-domain data sets, including accretion-powered pulsars, active galaxies, and variable stars (Kelly et al. 2014; Hu & Tak 2020; Elorrieta et al. 2021). Indeed, by way of illustration, Kelly et al. (2014) analysed *RXTE* data from the low-mass X-ray binary XTE 1550–564, whose compact object is a black hole rather than a neutron star, and concluded that its $L(t)$ fluctuations are consistent with a CARMA process of order (5, 4). The analysis

does not consider $\Omega(t)$, because $\Omega(t)$ cannot be measured for a black hole, and the generic CARMA(5, 4) process is not derived from a physical model of accretion.

The paper is structured as follows. In §2 we introduce the stochastic differential equations of motion, which govern how the state variables describing magnetocentrifugal accretion evolve, as well as the measurement equations, which relate the observables $\Omega(t)$ and $L(t)$ to the state variables, some of which are hidden. The equations are linearized about magnetocentrifugal equilibrium to prepare for implementing a Kalman filter. In §3 we set out a practical recipe for estimating the evolution of the state variables using a Kalman filter given the observed time series $\Omega(t)$ and $L(t)$. Validation tests with synthetic data are presented in §4, and the accuracy of parameter estimation is quantified approximately. Astrophysical implications are canvassed briefly in §5. Preliminary extensions of the analysis to generalized models of magnetocentrifugal accretion are introduced in the appendices. Applying the method to real astronomical data is postponed to future work, to be undertaken in collaboration with the X-ray timing community, which enjoys access to high-quality, calibrated data and specialized analysis software.

2. Accretion dynamics

Accretion from a disk onto a magnetized neutron star is a complicated, time-dependent process involving nonlinear feedback between the disk and magnetosphere, mediated by hydromagnetic instabilities at the disk-magnetosphere boundary, as seen in three-dimensional numerical simulations (Romanova et al. 2003, 2005; Kulkarni & Romanova 2008). The time series $\Omega(t)$ and $L(t)$ supplied by X-ray timing experiments do not contain enough information to infer uniquely the spatial structure in the simulations, e.g. the magnetic field geometry near the disk-magnetosphere boundary. In this paper, therefore, we model accretion in a spatially averaged manner within the successful magnetocentrifugal paradigm (Ghosh & Lamb 1979). In §2.1, we define and relate the two observables and four state variables that constitute the model, three of which are hidden, including the Maxwell stress at the disk-magnetosphere boundary, which is important physically and notoriously difficult to measure (Patruno & Watts 2021). The canonical magnetocentrifugal torque is written down in §2.2. The state of rotational equilibrium, about which the system fluctuates, and the stochastic driving forces which drive the system away from equilibrium are specified in §2.3 and §2.4 respectively. Linearized versions of the dynamical equations for the state variables and the measurement equations relating the observables to the state variables are presented in §2.5. The linearized equations are suitable for analysis with a Kalman filter.

2.1. Observables and state variables

Consider a hypothetical X-ray timing experiment targeting an accretion-powered pulsar. The experiment returns raw photon times of arrival, which are barycentered and converted into time series of the pulse period, $P(t_1), \dots, P(t_N)$, and the aperiodic X-ray luminosity, $L(t_1), \dots, L(t_N)$, using standard coherent timing methods, e.g. Fourier decomposition of the pulse profile and pulse folding (Bildsten et al. 1997; Patruno & Watts 2021; Serim et al. 2021).¹ The time series are sampled simultaneously at N epochs $t_1 \leq \dots \leq t_N$, spaced regularly or irregularly, during the interval $0 \leq t \leq T_{\text{obs}}$.²

Consider also the standard magnetocentrifugal model of disk accretion (Ghosh & Lamb 1979). Reformulated slightly from its canonical form, the model can be written in terms of four state variables, which are functions of time t . One state variable, the angular velocity $\Omega(t)$ of the neutron star, is related closely to $P(t)$, as discussed below. The other three state variables are hidden; they are related indirectly to $P(t)$ and $L(t)$ and cannot be measured directly. Let $S(t)$ denote the Maxwell stress at the disk-magnetsphere boundary, which opposes the ram pressure of the radially inflowing disk material (units: $\text{g cm}^{-1} \text{s}^{-2}$). Let $Q(t)$ be the rate at which mass flows from the accretion disk into the disk-magnetosphere boundary (units: g s^{-1}). Let $\eta(t)$ be the efficiency with which the gravitational potential energy of material falling onto the stellar surface is converted into X-rays (units: dimensionless). The roles played by $S(t)$, $Q(t)$, and $\eta(t)$ in the accretion dynamics are defined in §2.2 and §2.4. All quantities are expressed in CGS units.

The first step in formulating a Kalman filter is to relate the observables and state variables. The angular velocity of the star is essentially measured directly, viz.

$$P(t) = 2\pi/\Omega(t) + N_P(t) . \quad (1)$$

The additive measurement noise $N_P(t)$ is assumed to be Gaussian and white, with $\langle N_P(t_n) \rangle = 0$ and $\langle N_P(t_n)N_P(t_{n'}) \rangle = \Sigma_{PP}^2 \delta_{n,n'}$, where $\delta_{n,n'}$ denotes the Kronecker delta. Note that Σ_{PP} has units of s. Equation (1) is a reasonable starting point for estimating the parameters of the magnetocentrifugal model. However it is an approximation; the discovery of (anti)correlations between pulse phase residuals and X-ray flux (instead of $\dot{\Omega}$ and X-ray flux) in several accretion-powered pulsars (Patruno et al. 2009) implies that the pulse frequency

¹The luminosity $L(t)$ is discussed for notational convenience in this paper. In practice, the analysis does not rely on knowing the distance D to the source. One can work instead with the aperiodic X-ray flux $F_X(t) = L(t)/(4\pi D^2)$ and rescale the parameters to be estimated accordingly by powers of D .

²The signal processing framework in this paper can be generalized to handle nonsimultaneous sampling of the two time series, if there is demand in the future (Gelb 1974).

derivative does not equal the spin frequency derivative exactly (Riggio et al. 2008; Patruno & Watts 2021). That is, one has $\langle \Omega(t) \rangle \neq 2\pi/\langle P(t) \rangle$ in some circumstances, contradicting (1), perhaps due to secular hot spot migration driven by disk-magnetosphere instabilities (Romanova et al. 2003; Kulkarni & Romanova 2008).

The measured X-ray luminosity can be related indirectly to the mass accretion rate and radiative efficiency by the usual energy conservation formula, viz.

$$L(t) = GMQ(t)\eta(t)/R + N_L(t) . \quad (2)$$

The additive measurement noise $N_L(t)$ is assumed to be Gaussian and white, with $\langle N_L(t_n) \rangle = 0$ and $\langle N_L(t_n)N_L(t_{n'}) \rangle = \Sigma_{LL}^2 \delta_{n,n'}$. If there is reason to believe that $N_P(t_n)$ and $N_L(t_n)$ are correlated through the measurement process, it is straightforward to generalize the analysis to accommodate $\langle N_P(t_n)N_L(t_{n'}) \rangle = \Sigma_{PL}^2 \delta_{n,n'} \neq 0$. In (2), $\eta(t)$ is the fraction of the specific gravitational potential energy GM/R converted to X-rays, when infalling matter strikes the stellar surface, M and R denote the mass and radius of the star respectively, and G denotes Newton’s gravitational constant. A one-to-one correspondence is assumed sometimes between $L(t)$ and $Q(t)$, with $\eta(t) = 1$ in (2). In this paper we allow $\eta(t)$ to fluctuate in the range $0 < \eta(t) < 1$ (Sanna et al. 2017). Partly the fluctuations arise from radiative processes: how much of the gravitational potential energy is converted into heat and hence X-rays? Partly they arise from nonconservative mass transfer: how much of $Q(t)$ lands on the stellar surface, and how much is directed into an outflow (Marino et al. 2019)? An idealized, phenomenological model of the $\eta(t)$ dynamics is introduced in §2.4.

2.2. Magnetocentrifugal torque

In the canonical magnetocentrifugal picture of accretion (Ghosh & Lamb 1979), there are two characteristic radii. The Alfvén radius, $R_m(t)$, defines the disk-magnetosphere boundary. It is located where the magnetospheric Maxwell stress balances the disk ram pressure, viz. $S \approx \rho v^2$, where $\rho = Q/(4\pi R_m^2 v)$ and $v = (GM/R_m)^{1/2}$ are the mass density and infall speed respectively in a cylindrically symmetric inflow approximately in free fall. In terms of the hidden state variables, the stress balance condition translates to

$$R_m(t) = (4\pi)^{-2/5} (GM)^{1/5} Q(t)^{2/5} S(t)^{-2/5} . \quad (3)$$

The corotation radius, $R_c(t)$, is located where the Kepler frequency equals the angular velocity of the star, viz.

$$R_c(t) = (GM)^{1/3} \Omega(t)^{-2/3} . \quad (4)$$

The fastness parameter $(R_m/R_c)^{3/2}$ controls the sign of the magnetocentrifugal torque on the star. For $R_m < R_c$, material at the disk-magnetosphere boundary orbits faster than the star rotates. Some fraction [related but not equal to $\eta(t)$] falls onto the star and spins it up through a combination of hydromagnetic and mechanical torques. For $R_m > R_c$, in the propeller phase, the material at the disk-magnetosphere boundary orbits slower than the star rotates. It is flung outwards centrifugally by the corotating magnetosphere and spins down the star. Importantly, some material can still accrete onto the stellar surface during the propeller phase for $1 \lesssim R_m/R_c \lesssim 3$, even if the remainder is diverted into an outflow (Papitto & Torres 2015; Marino et al. 2019; Patruno & Watts 2021). Consequently the net torque involves both hydromagnetic and mechanical components in general. The equation of motion for $\Omega(t)$ then reads

$$\frac{d\Omega}{dt} = \frac{(GM)^{1/2}}{I} \left\{ 1 - \left[\frac{R_m(t)}{R_c(t)} \right]^{3/2} \right\} R_m(t)^{1/2} Q(t) , \quad (5)$$

where I denotes the star’s moment of inertia.

In this paper, for the sake of simplicity, we neglect modifications of (5) due to radiation pressure (Andersson et al. 2005; Haskell et al. 2015), magnetic dipole braking in quiescence (Patruno 2010; Papitto et al. 2011; Melatos & Mastrano 2016), and gravitational radiation reaction (Bildsten 1998; Melatos & Payne 2005). The modifications are straightforward to make, whenever the data are detailed enough to warrant their inclusion. We also neglect disk warping and precession, caused by misalignment between the magnetic and rotation axes of the star and the angular momentum vector of the disk (Foucart & Lai 2011; Lai 2014; Romanova et al. 2021); see Figures 6 and 11 in Romanova et al. (2021) for a vivid illustration of how warping and precession cause variability in $Q(t)$. Misalignment necessarily leads to complicated, three-dimensional flows (Romanova et al. 2021), whose description lies outside the scope of this paper.

2.3. Magnetocentrifugal equilibrium

Rotational equilibrium corresponds to zero torque, which is achieved for $R_c(t) = R_m(t) = R_{m0} = \text{constant}$, $S(t) = S_0 = \text{constant}$, $Q(t) = Q_0 = \text{constant}$, $\eta(t) = \eta_0 = \text{constant}$, and $\Omega(t) = \Omega_0 = \text{constant}$, with

$$\Omega_0 = (4\pi)^{3/5} (GM)^{1/5} Q_0^{-3/5} S_0^{3/5} \quad (6)$$

and

$$L_0 = GMQ_0\eta_0/R . \quad (7)$$

Often it is useful to write S_0 and R_{m0} in terms of the star’s magnetic moment μ (units: G cm^3), assuming a dipole magnetic field and hence $S_0 = (2\pi)^{-1}\mu^2 R_{m0}^{-6}$ inside the magnetosphere. The results are $S_0 = 2^{-19/7}\pi^{-1}(GM)^{6/7}\mu^{-10/7}Q_0^{12/7}$, $R_{m0} = 2^{2/7}(GM)^{-1/7}\mu^{4/7}Q_0^{-2/7}$ (a familiar expression in the literature), and hence

$$\mu = 2^{-1/2}(GM)^{5/6}\Omega_0^{-7/6}Q_0^{1/2}. \quad (8)$$

In this paper, we assume that μ is constant for simplicity. However there is theoretical (Shibazaki et al. 1989; Payne & Melatos 2004; Zhang & Kojima 2006) and observational (Patruno 2012) evidence, that polar magnetic burial reduces μ in the short term, during accretion episodes, and in the long term, as reflected in the spin distribution of accretion-powered pulsars (Priymak et al. 2011; Wang et al. 2011).

The four-dimensional state vector in equilibrium, $(\Omega_0, Q_0, S_0, \eta_0)$, is a key input into the Kalman filter, as described in §3. However, the two time-averaged observables $\Omega_0 = \langle 2\pi/P(t) \rangle$ and $L_0 = \langle L(t) \rangle$, and the magnetocentrifugal equilibrium condition $R_c(t) = R_m(t)$, contain only three independent pieces of information. One is therefore left with two approaches to solve for the four components of $(\Omega_0, Q_0, S_0, \eta_0)$: (I) assume a plausible theoretical value for one component, e.g. $\eta_0 = 0.5$; or (II) exploit the time-dependent information in $P(t)$ and $L(t)$, not just $\langle P(t) \rangle$ and $\langle L(t) \rangle$, and include one component in the Kalman filter as an unknown to be estimated. Approach II is preferable as it is more general. Handy formulas for the components of $(\Omega_0, Q_0, S_0, \eta_0)$ following either approach are presented in Appendix A for the convenience of the reader.

Many accretion-powered pulsars exist in a state of disequilibrium (Bildsten et al. 1997; Yang et al. 2017; Mushtukov & Tsygankov 2022; Serim et al. 2022). They spin up or down secularly over long intervals, typically lasting years, with $|R_c(t) - R_m(t)| \gtrsim R_c(t)$. Examples include Her X–1 and 4U 1626–67, which accrete via Roche lobe overflow, where the secular intervals last $\gtrsim 10$ yr (Serim et al. 2022). For such systems, it is inappropriate to linearize (5) about $R_c(t) = R_m(t) = R_{m0}$, as in §2.5, in order to apply a linear Kalman filter. Instead, in the absence of an accepted analytic theory of torque transitions (Nelson et al. 1997; van Kerkwijk et al. 1998; Locsei & Melatos 2004; Lai 2014; Gençali et al. 2022), it makes sense to analyze each decade-long secular interval separately, by applying a nonlinear (e.g. unscented) Kalman filter (Julier & Uhlmann 1997) to (5) in its nonlinear form. An illustrative worked example is presented in Appendix B for completeness.

2.4. Stochastic fluctuations

Accretion-powered pulsars are stochastic systems. Partly the stochasticity is driven externally, e.g. flicker noise due to propagating fluctuations in the disk α parameter on the viscous time-scale (Lyubarskii 1997), or longer-term $Q(t)$ modulation as the companion star evolves. Partly the stochasticity emerges internally due to nonlinear feedback loops, e.g. self-healing Rayleigh-Taylor instabilities at the disk-magnetosphere boundary (Romanova et al. 2003; Kulkarni & Romanova 2008; Das et al. 2022), or cyclic accretion due to disk trapping at the magnetocentrifugal barrier (D’Angelo & Spruit 2012). In this paper, we focus on internal stochasticity, specifically mean-reverting fluctuations around magnetocentrifugal equilibrium.

Hydromagnetic processes at the disk-magnetosphere boundary cannot be observed directly. The physics depends on the spatial structure of the magnetic field, which is too complicated to be inferred uniquely from X-ray timing measurements of $P(t)$ and $L(t)$. Three-dimensional hydromagnetic simulations are expensive computationally and cannot be repeated often enough to predict ensemble statistics of hidden state variables reliably, e.g. the PSD of $S(t)$ (Romanova et al. 2003; Kulkarni & Romanova 2008). Accordingly, we adopt an idealized, phenomenological dynamical model, in which the hidden state variables $Q(t)$, $S(t)$, and $\eta(t)$ execute mean-reverting random walks driven by white noise (de Kool & Anzer 1993). That is, $Q(t)$, $S(t)$, and $\eta(t)$ satisfy the Langevin equations

$$\frac{dQ}{dt} = -\gamma_Q[Q(t) - Q_0] + \xi_Q(t) , \quad (9)$$

$$\frac{dS}{dt} = -\gamma_S[S(t) - S_0] + \xi_S(t) , \quad (10)$$

$$\frac{d\eta}{dt} = -\gamma_\eta[\eta(t) - \eta_0] + \xi_\eta(t) , \quad (11)$$

where γ_Q^{-1} , γ_S^{-1} , and γ_η^{-1} are characteristic time-scales of mean reversion, and $\xi_Q(t)$, $\xi_S(t)$, and $\xi_\eta(t)$ are white-noise driving terms with ensemble statistics $\langle \xi_A(t) \rangle = 0$ and

$$\langle \xi_A(t) \xi_{A'}(t') \rangle = \sigma_{AA'}^2 \delta(t - t') , \quad (12)$$

i.e. delta-correlated in time, with $A, A' \in \{Q, S, \eta\}$.³ In this paper, we assume $\sigma_{AA'} = 0$ for $A \neq A'$ for the purpose of illustration, and to keep the number of unknown parameters

³The equations of motion (9)–(11) describe a continuous-time, Ornstein-Uhlenbeck process (Gardiner 1994), whereas the measurement equations (1) and (2) are sampled at the discrete epochs $t_1 \leq \dots \leq t_N$. Hence $\langle \xi_A(t) \xi_{A'}(t') \rangle$ in (12) is proportional to the Dirac delta function $\delta(t - t')$, whereas $\langle N_B(t_n) N_{B'}(t_{n'}) \rangle$ in §2.1 is proportional to the Kronecker delta $\delta_{n,n'}$ for $B, B' \in \{P, L\}$. The units of $\sigma_{AA'}^2$ in (12) are the units of A multiplied by the units of A' divided by seconds, whereas the units of $\Sigma_{BB'}^2$ in §2.1 are the units of B multiplied by the units of B' .

manageable. Cross-correlations of the form $\sigma_{AA'} \neq 0$ for $A \neq A'$ are straightforward to add in the future, if astronomical data demand their inclusion.

The Langevin equations (9)–(12) ensure that $Q(t)$, $S(t)$, and $\eta(t)$ wander randomly about their equilibrium values without drifting secularly, with root-mean-square fluctuations $\sim \gamma_Q^{-1/2} \sigma_{QQ}$, $\gamma_S^{-1/2} \sigma_{SS}$, and $\gamma_\eta^{-1/2} \sigma_{\eta\eta}$ respectively. For example, the probability density function for $Q(t)$ in the limit $t \rightarrow \infty$ takes the form $p(Q) \propto \exp[-\gamma_Q(Q - Q_0)^2/\sigma_{QQ}^2]$. Analogous formulas apply for $p(S)$ and $p(\eta)$. Formally (9)–(12) allow for unphysical fluctuations with $Q, S, \eta < 0$ or $\eta > 1$. In practice, however, the probabilities of such fluctuations are exponentially small, as one has $\gamma_Q^{-1/2} \sigma_{QQ} \ll Q_0$, $\gamma_S^{-1/2} \sigma_{SS} \ll S_0$, and $\gamma_\eta^{-1/2} \sigma_{\eta\eta} \ll \eta_0$ in accretion-powered pulsars in their active phase. There is no observational evidence that the disk-magnetosphere system is disrupted catastrophically, e.g. $Q < 0$ (accretion ceases) or $S < 0$ (Maxwell stress vanishes). Systems in quiescence are not considered here (Patruno & Watts 2021). The approximation (9)–(12) simplifies the Kalman filter considerably (see §3).

We emphasize that (9)–(12) are highly idealized in important respects. For example, it is likely that $\xi_S(t)$ and $\xi_\eta(t)$ are anticorrelated to some degree, with $\sigma_{S\eta} \neq 0$. Simulations show that Rayleigh-Taylor instabilities at the disk-magnetosphere boundary open up transient magnetic channels, accompanied by fluctuations in $S(t)$, which temporarily permit “fingers” of disk material to break through the magnetosphere and strike the stellar surface, before the channels close, and equilibrium is restored (Romanova et al. 2003, 2005; Kulkarni & Romanova 2008). This gating process is correlated with the nonradiative component of $\eta(t)$, i.e. the component associated with nonconservative mass transfer as discussed in §2.1 and §2.2. When the Rayleigh-Taylor channels close, and $S(t)$ fluctuates above S_0 , some fraction of $Q(t)$ is redirected magnetocentrifugally into an outflow, and $\eta(t)$ fluctuates below η_0 (Marino et al. 2019; Patruno & Watts 2021).⁴ As noted above, it is straightforward to implement $\sigma_{S\eta} \neq 0$ through (12) in future work, at the cost of introducing an additional parameter, if the data warrant.

A second idealization is that $\xi_Q(t)$, $\xi_S(t)$, and $\xi_\eta(t)$ obey white noise statistics. X-ray timing experiments indicate that some objects exhibit red noise in the torque $\dot{P}(t)$ (Bildsten et al. 1997; Serim et al. 2022) and light curve $L(t)$ (Mukherjee et al. 2018). We emphasize that red noise is consistent with (9)–(12): although $\xi_Q(t)$, $\xi_S(t)$, and $\xi_\eta(t)$ are white, the PSDs of $Q(t)$, $S(t)$, and $\eta(t)$ are red, because $\xi_Q(t)$, $\xi_S(t)$, and $\xi_\eta(t)$ appear in the derivatives dQ/dt , dS/dt , and $d\eta/dt$, and the deterministic terms on the right-hand sides of (9)–(12)

⁴The anticorrelation is imperfect for two reasons. First, the magnetic geometry at the disk-magnetosphere boundary is complicated, and $S(t)$ does not always decrease, when a Rayleigh-Taylor channel opens. Second, $\eta(t)$ contains a radiative component (the fraction of the gravitational potential energy converted into heat and hence X-rays, when matter strikes the stellar surface), which does not depend on $S(t)$.

act as low-pass filters on the long time-scales γ_Q^{-1} , γ_S^{-1} , and γ_η^{-1} respectively, cf. Baykal & Oegelman (1993). The red noise feeds into $\Omega(t)$ and hence the observables $P(t)$ and $L(t)$ through (1), (2), and (5). Nonetheless, the shapes (e.g. power-law index) of the PSDs of $P(t)$ and $L(t)$ are not reproduced in detail by (9)–(12) in some objects (Serim et al. 2022). We persevere with (9)–(12) in this introductory paper by way of illustration, while noting that the model can be generalized easily, when the data demand, by augmenting (9)–(12) with additional filters to generate noise with the desired color (Kelly et al. 2014; Hu & Tak 2020; Elorrieta et al. 2021).

Data volumes available at present ($N \lesssim 10^3$) are insufficient to constrain dynamical models of the disk-magnetosphere boundary that are more realistic than (5) and (9)–(11). Yet there is no doubt that (5) and (9)–(11) oversimplify many important aspects of the accretion physics, beyond those highlighted in the previous two paragraphs. For example, the Maxwell stress is a tensor not a scalar, forces perpendicular to the disk cannot be neglected, and the transition from spin up ($R_m < R_c$) to spin down ($R_m > R_c$) occurs more abruptly than implied by (5). We discuss the implications of these and other approximations in Appendix C and sketch out, for the sake of completeness, how the Kalman filter framework can be refined to accommodate some of these effects in the future, when more data become available. Specifically, we present generalized versions of (5) and (9)–(11), that describe an abrupt propeller transition and disk trapping (D’Angelo & Spruit 2012; D’Angelo 2017), albeit still in an idealized form, and sketch out how to analyze the generalized models with an unscented Kalman filter (Julier & Uhlmann 1997).

2.5. Linearized equations of motion and measurement equations

The analysis in this paper applies to accretion-powered pulsars whose fluctuations about magnetocentrifugal equilibrium are small, with $\gamma_Q^{-1/2}\sigma_{QQ} \ll Q_0$, $\gamma_S^{-1/2}\sigma_{SS} \ll S_0$, and $\gamma_\eta^{-1/2}\sigma_{\eta\eta} \ll \eta_0$ as discussed in §2.4. Small fluctuations can be treated with a linear Kalman filter (see §3). Ultimately detailed comparisons with observational data will be needed to assess whether or not the linear approximation is accurate in individual objects. Evidence exists for nonlinearity in dynamical models of other accreting systems, such as black hole binaries (Timmer et al. 2000; Mannattil et al. 2016) and cataclysmic variables (Scaringi et al. 2014). Quiescent systems, and catastrophic events such as disk disruption or magnetospheric collapse, are not considered here.

Let us denote perturbed fractional quantities with the subscript ‘1’ and unperturbed absolute quantities with the subscript ‘0’ (see §2.3). For example, we write $\Omega_1(t) = [\Omega(t) - \Omega_0]/\Omega_0$, $Q_1(t) = [Q(t) - Q_0]/Q_0$, and so on. Linearizing the equations of motion (3)–(5) and

(9)–(11) yields

$$\frac{d}{dt} \begin{pmatrix} \Omega_1 \\ Q_1 \\ S_1 \\ \eta_1 \end{pmatrix} = \begin{pmatrix} -\gamma_\Omega & -3\gamma_\Omega/5 & 3\gamma_\Omega/5 & 0 \\ 0 & -\gamma_Q & 0 & 0 \\ 0 & 0 & -\gamma_S & 0 \\ 0 & 0 & 0 & -\gamma_\eta \end{pmatrix} \begin{pmatrix} \Omega_1 \\ Q_1 \\ S_1 \\ \eta_1 \end{pmatrix} + \begin{pmatrix} 0 \\ Q_0^{-1}\xi_Q \\ S_0^{-1}\xi_S \\ \eta_0^{-1}\xi_\eta \end{pmatrix}, \quad (13)$$

with

$$\gamma_\Omega = \frac{(GM)^{1/2} R_{m0}^{1/2} Q_0}{I\Omega_0}. \quad (14)$$

Linearizing the measurement equations (1) and (2) yields

$$P_1 = -\Omega_1 + P_0^{-1}N_P \quad (15)$$

and

$$L_1 = Q_1 + \eta_1 + L_0^{-1}N_L, \quad (16)$$

with $P_1(t) = [P(t) - P_0]/P_0$, $L_1(t) = [L(t) - L_0]/L_0$, and $P_0 = 2\pi/\Omega_0$. Equations (13)–(16) are in the correct format for analysis with a linear Kalman filter.

3. Kalman filter

The equations of motion (13) and (14), and the measurement equations (15) and (16), can be applied directly to observational data with the goal of estimating the model parameters using a Kalman filter. The inputs and outputs are laid out in §3.1, together with a step-by-step recipe for performing the analysis. The implementation of the parameter estimation algorithm, which combines a Kalman filter with a nested sampler, is outlined in §3.2. The reader is referred to Meyers et al. (2021) for details.

3.1. Inputs and outputs

The analysis takes as inputs the measured data as well as astrophysical priors on the model parameters. The measurements comprise two time series, $P(t_n)$ and $L(t_n)$, each containing N samples at times t_n ($1 \leq n \leq N$). The priors are left to the discretion of the analyst. Certain model parameters appear combined inextricably as products in (13)–(16) and cannot be estimated independently. They comprise M , R , I , and one component of (Q_0, S_0, η_0) , if the analysis follows approach I in Appendix A. They comprise M , R , and I only, if the analysis follows approach II in Appendix A. In this paper, we follow approach

II, as it is more general, and assign plausible, fiducial values to M , R , and I for the sake of definiteness.

Under approach II, the analysis returns as outputs the posteriors on the seven model parameters $\Theta = (\gamma_\Omega, \gamma_A, \sigma_{AA})$, with $A \in \{Q, S, \eta\}$, as well as an error-minimizing estimate of the time series $\hat{\mathbf{X}}(t_n)$, where $\mathbf{X} = (\Omega_1, Q_1, S_1, \eta_1)$ is the state vector. The latter time series is potentially valuable for studying the hidden physical processes governing magnetospheric variables such as the Maxwell stress $S(t)$ at the disk-magnetosphere boundary.

A recipe to conduct the analysis proceeds as follows.

1. Calculate $\Omega_0 = N^{-1} \sum_{n=1}^N 2\pi/P(t_n)$ and $L_0 = N^{-1} \sum_{n=1}^N L(t_n)$. These parameters enter the model through (13)–(16).
2. Generate the time series $P_1(t_n) = P(t_n) - 2\pi/\Omega_0$ and $L_1(t_n) = L(t_n) - L_0$.
3. Decide what model parameters to fix. Under approach II in Appendix A, one assumes plausible fiducial values for M , R , and I , writes Q_0 , S_0 , and η_0 in terms of γ_Ω according to (A4)–(A6), and sets the parameter vector of the Kalman filter to be $\Theta = (\gamma_\Omega, \gamma_A, \sigma_{AA})$, with $A \in \{Q, S, \eta\}$.
4. Run a nested sampler like `dynesty` (Speagle 2020) with the Kalman filter likelihood defined in §3.2 to estimate Θ . A formal identifiability analysis (Bellman & Åström 1970) presented in Appendix D, and empirical tests on synthetic data presented in §4, confirm that the seven components of Θ can be estimated unambiguously.
5. Given Θ , estimate the time series $\hat{\mathbf{X}}(t_n)$ of the hidden state variables.

3.2. Implementation

Equations (13)–(16) take the standard form of a linear Kalman filter (Kalman 1960; Gelb 1974). The state space representation, recursion relations, and Bayesian likelihood of a Kalman filter are written down and justified thoroughly in Section 3 and Appendices B–D in Meyers et al. (2021). The discussion is not repeated here in full. The only slightly nonstandard feature of our application is that X-ray timing experiments measure photon times of arrival, which must be converted to $P(t_n)$ before use.

The nested sampler evaluates the log-likelihood associated with the Kalman filter (Mey-

ers et al. 2021)

$$\ln p(\{\mathbf{Y}_n\}_{n=1}^N | \Theta) = -\frac{1}{2} \sum_{n=1}^N [D_{\mathbf{Y}} \ln(2\pi) + \ln \det(\mathbf{s}_n) + \mathbf{e}_n^T \mathbf{s}_n^{-1} \mathbf{e}_n] , \quad (17)$$

where $\mathbf{Y}_n = [P_1(t_n), L_1(t_n)]$ is the measurement vector, $D_{\mathbf{Y}} = 2$ is the dimension of \mathbf{Y}_n , and \mathbf{e}_n and $\mathbf{s}_n = \langle \mathbf{e}_n \mathbf{e}_n^T \rangle$ (Einstein summation convention suspended temporarily) are the innovation vector and its covariance matrix respectively. The nested sampler proceeds iteratively. It selects an estimate $\hat{\Theta}$, runs the Kalman filter, computes (17), refines $\hat{\Theta}$, and repeats. Note that \mathbf{s}_n contains information about the measurement noise, which is known (Σ_{PP}, Σ_{LL}), and the process noise, which is parametrized by σ_{QQ}, σ_{SS} , and $\sigma_{\eta\eta}$ and estimated.

The innovation vector is generated at every time step t_n by the Kalman filter from the measurements and the state estimate $\hat{\mathbf{X}}_n$. One computes

$$\mathbf{e}_n = \mathbf{Y}_n - \mathbf{C} \exp[\mathbf{A}(t_n - t_{n-1})] \hat{\mathbf{X}}_{n-1} , \quad (18)$$

where \mathbf{C} is the 2×4 matrix defined implicitly through $\mathbf{Y} = \mathbf{C}\mathbf{X} + (P_0^{-1}N_P, L_0^{-1}N_L)$ in (15) and (16). The state vector is updated recursively via

$$\hat{\mathbf{X}}_n = \exp[\mathbf{A}(t_n - t_{n-1})] \hat{\mathbf{X}}_{n-1} + \mathbf{k}_n \mathbf{e}_n , \quad (19)$$

where \mathbf{A} is the 4×4 matrix in (13) (constant with n in this application), and \mathbf{k}_n is the Kalman gain defined to minimize the squared error $|\mathbf{X}_n - \hat{\mathbf{X}}_n|^2$. The Kalman filter returns an estimate of the squared error at t_n as part of its output. An expression for the Kalman gain is provided in standard textbooks (Gelb 1974); see also (A6) in Appendix A in Kelly et al. (2014) and (C5) in Appendix C in Meyers et al. (2021).

4. Validation with synthetic data

In this section, we lead the reader through a validation test conducted on synthetic data. We set out the parameters of a representative test source in §4.1. We then investigate the accuracy with which the Kalman filter and nested sampler track the state evolution and estimate the source parameters in §4.2 and §4.3 respectively. The synthetic data are generated by solving the nonlinear equations of motion (5) and (9)–(11) with the Runge-Kutta Itô integrator (Rößler 2010) in the Python package `sdeint`⁵ and passing the output through the nonlinear measurement equations (1) and (2) to produce the time series $P(t_n)$ and $L(t_n)$

⁵<https://github.com/mattja/sdeint>

for $1 \leq n \leq N$. The validation test serves two purposes: (i) it gives an approximate sense of how accurately one can recover Θ given a representative volume of data from a representative source; and (ii) it is a worked example which illustrates end-to-end the practical steps in a typical analysis. A fuller study of the accuracy of the Kalman filter is postponed, until the systematic (e.g. calibration) uncertainties associated with real astronomical data are characterized better through collaboration with the X-ray timing community.

4.1. Representative test source

As a representative example, we consider the following hypothetical source: an accretion-powered pulsar with equilibrium mass accretion rate $Q_0 = 3.9 \times 10^{13} \text{ g s}^{-1}$ and dipole magnetic moment $\mu = 3.0 \times 10^{30} \text{ G cm}^3$. The source parameters are recorded in Table 1. The components of the equilibrium state vector $(\Omega_0, Q_0, S_0, \eta_0)$ appear in the first four lines of the table and satisfy the conditions of magnetocentrifugal equilibrium in §2.3. Observational studies of $L(t)$ and $P(t)$ fluctuations in objects undergoing disk accretion point to relaxation processes operating on time-scales of days to weeks (Bildsten et al. 1997; Mukherjee et al. 2018; Serim et al. 2021), e.g. the Lomb-Scargle PSD computed from the *RXTE* light curve of Scorpius X–1 rolls over at $\sim 10^{-7} \text{ s}^{-1}$ (Mukherjee et al. 2018), as does the PSD of $P(t_n)$ fluctuations measured in 2S 1417–624; see Figure 6 in Serim et al. (2021). Hence, in the middle section of the table, we take $1 \leq \gamma_A / (10^{-7} \text{ s}^{-1}) \leq 5$ with $A \in \{Q, S, \eta\}$ as a typical range.⁶ The noise amplitudes are then chosen to give fractional fluctuations of $\lesssim 10\%$ in the hidden state variables, with $\gamma_Q^{-1/2} \sigma_{QQ} = 0.1Q_0$, $\gamma_S^{-1/2} \sigma_{SS} = 0.1S_0$, and $\gamma_\eta^{-1/2} \sigma_{\eta\eta} = 0.1\eta_0$. Fractional fluctuations of this order are broadly consistent with observations (Serim et al. 2021), e.g. one infers $\sigma_{QQ} \approx 0.4Q_0\gamma_Q^{1/2}$ from Figure 3 in Mukherjee et al. (2018).⁷ Finally the measurement noises $N_P(t)$ and $N_L(t)$ are chosen to be Gaussian for simplicity and to correspond to $1\text{-}\sigma$ error bars of 10^{-6} and 10^{-2} per cent on $P_1(t_n)$ and $L_1(t_n)$ respectively.⁸ The error bars are deliberately conservative with respect to the brightest objects, where the Kalman filter is likely to be tested first, as gauged from the top-right corner of Figure 4

⁶The parameters Θ cannot be estimated uniquely by the Kalman filter in the special case $\gamma_Q = \gamma_\eta$, which is therefore avoided in §4; see the formal identifiability analysis in Appendix D.

⁷Translating $L(t)$ fluctuations directly to $Q(t)$ fluctuations via (2) with $\eta(t) = \eta_0 = \text{constant}$ is an approximation, suitable for making *a priori* order-of-magnitude estimates. A self-consistent analysis involves running the Kalman filter in §3 or its equivalent.

⁸ $N_L(t)$ is a random error. It does not include systematic errors, e.g. arising from the conversion of X-ray flux to luminosity. In a real, astronomical analysis, one works with $F_X(t)$ instead of $L(t)$, and the distance D to the source cannot be inferred by the Kalman filter, just like M , R , and I ; see footnote 1.

in Serim et al. (2021). They illustrate the most challenging parameter estimation scenario, where the fractional amplitude of some components of the measurement noise is comparable to the fractional amplitude of the dynamical fluctuations in some hidden state variables.

Quantity	Value	Units
Ω_0	2.2×10^{-2}	rad s ⁻¹
Q_0	3.9×10^{13}	g s ⁻¹
S_0	9.3×10^0	g cm ⁻¹ s ⁻²
η_0	0.50	—
M	2.8×10^{33}	g
R	1.0×10^6	cm
I	8.4×10^{44}	g cm ²
γ_Q	1.0×10^{-7}	s ⁻¹
γ_S	3.0×10^{-7}	s ⁻¹
γ_η	5.0×10^{-7}	s ⁻¹
σ_{QQ}	1.3×10^9	g s ^{-3/2}
σ_{SS}	5.4×10^{-4}	g cm ⁻¹ s ^{-5/2}
$\sigma_{\eta\eta}$	3.5×10^{-5}	s ^{-1/2}
N	500	—
T_{obs}	3.0×10^8	s
Σ_{PP}	2.9×10^{-6}	s
Σ_{LL}	3.7×10^{29}	g cm ² s ⁻³

Table 1: Injected parameters of a representative accretion-powered pulsar for the validation tests in §4. The top, middle, and bottom sections contain equilibrium, fluctuation, and measurement parameters respectively. The epochs $0 \leq t_1 \leq \dots \leq t_N = T_{\text{obs}}$ are spaced equally for the sake of illustration. Derived parameters: $R_{\text{m}0} = 7.3 \times 10^9$ cm, $\mu = 3.0 \times 10^{30}$ G cm³, $\gamma_\Omega = 2.5 \times 10^{-12}$ s⁻¹, $P_0 = 2.9 \times 10^2$ s, $L_0 = 3.7 \times 10^{33}$ g cm² s⁻³.

4.2. State tracking

Figure 1 presents the inputs and outputs of the Kalman filter as functions of time for the hypothetical source in Table 1. The top two panels display the synthetic measurements $P_1(t_n)$ and $L_1(t_n)$ for $1 \leq n \leq 500$.⁹ Broadly speaking, the spin and flux wandering resemble

⁹The sampling epochs t_n are spaced equally for the sake of illustration, but the formulas in §3 do not presuppose equal spacing.

visually and qualitatively what one sees in real data (Bildsten et al. 1997; Mukherjee et al. 2018; Serim et al. 2021). The bottom four panels display the four components of the state vector estimated by the Kalman filter, $\hat{\mathbf{X}}_n = [\hat{\Omega}_1(t_n), \hat{Q}_1(t_n), \hat{S}_1(t_n), \hat{\eta}_1(t_n)]$, for $1 \leq n \leq 500$. In all four panels, there is close agreement between the estimated component (colored, solid curve) and the injected component generated by solving (5) and (9)–(11) numerically (black, dashed curve). That is, the Kalman filter performs creditably in reconstructing the evolution of the hidden state variables $Q(t)$, $S(t)$, and $\eta(t)$, which cannot be observed directly. The accuracy of the reconstruction is quantified in §4.3.

We draw the reader’s attention to two points of physical interest in Figure 1. First, the mean-reverting nature of the hidden variables is clear upon inspecting the bottom three panels. The characteristic time-scale shortens visibly from $\gamma_Q^{-1} = 1.0 \times 10^7$ s in the fourth panel to $\gamma_\eta^{-1} = 2.0 \times 10^6$ s in the sixth panel, while the fractional root-mean-square amplitude $\approx \gamma_A^{-1/2} \sigma_{AA} = 0.1$ with $A \in \{Q, S, \eta\}$ is the same in the fourth, fifth, and sixth panels, as expected from Table 1. Second, the fractional amplitudes of the fluctuations $P_1(t_n)$ (top panel) and $\Omega_1(t_n)$ (third panel) are $\approx \gamma_A/\gamma_\Omega \sim 10^5$ times smaller (with $A \in \{Q, S, \eta\}$) than the fluctuations in the other panels; note the different scales on the axes. This occurs because $\sim 10\%$ fluctuations in the torque, driven by comparable fluctuations in the three hidden variables, translate into smaller (and slower) fluctuations in the spin, due to the star’s large moment of inertia. The effect is quantified analytically in Appendix D; see equations (D6)–(D11).

4.3. Parameter estimation and its accuracy

Figure 2 presents the posterior distribution of the seven parameters $\Theta = (\gamma_\Omega, \gamma_A, \sigma_{AA})$, with $A \in \{Q, S, \eta\}$, returned by the nested sampler in §3. The mode of the posterior corresponds to the optimal estimated state sequence $\hat{\mathbf{X}}_n$ plotted in Figure 1. The seven-dimensional posterior is visualized in cross-section through a traditional corner plot. All seven parameters are estimated unambiguously and accurately. This empirical finding confirms the prediction of a formal identifiability analysis, a standard tool in electrical engineering (Bellman & Åström 1970), which is presented in Appendix D.¹⁰ The one-dimensional posteriors (histograms) in Figure 2 are unimodal and peak near the injected parameter values indicated by the blue lines, with the absolute error in the peak ranging from a minimum

¹⁰In many systems, certain parameters cannot be estimated unambiguously. For example, radio timing data are insufficient in general to identify all six parameters of the classic, two-component, crust-superfluid model of a pulsar exhibiting timing noise; see Meyers et al. (2021).

of ≈ 0.025 dex for γ_Q to a maximum of ≈ 0.15 dex for γ_Ω . Likewise the two-dimensional posteriors (contour plots) are unimodal and peak near the injection (intersection of the blue lines). The full width half maximum ranges from ≈ 0.10 dex for σ_{QQ} and σ_{SS} to ≈ 0.60 dex for γ_Ω . The parameters in Θ are largely uncorrelated. Arguably there are hints of γ_Ω - $\sigma_{\eta\eta}$ and σ_{QQ} - $\sigma_{\eta\eta}$ anticorrelations, visible as a diagonal tilt of the innermost contours in the γ_Ω - $\sigma_{\eta\eta}$ and σ_{QQ} - $\sigma_{\eta\eta}$ planes, but their significance is marginal.

The results in Figures 1 and 2 refer to a single, random realization of the noisy measurements $P(t_n)$ and $L(t_n)$. How representative are they, if the experiment is repeated? Figure 3 demonstrates how accurately the Kalman filter and nested sampler recover the injected values of the fluctuation parameters γ_A (left panel) and σ_{AA}/A_0 (right panel; normalized by the equilibrium value A_0) in Table 1, for $A \in \{Q, S, \eta\}$ color-coded as per the caption, by analysing 200 random realizations of the noisy measurements. Each variable is plotted in cgs units on a log scale. All six histograms peak near the injected values, indicated by dashed, color-coded, vertical lines. The absolute error in the peak ranges from ≈ 0.010 dex for γ_Q to ≈ 0.11 dex for γ_η . Moreover the dispersion is modest. The full width half maximum ranges from ≈ 0.12 dex for $\sigma_{\eta\eta}$ to ≈ 0.60 dex for γ_Q . Extreme outliers (e.g. when the nested sampler fails to converge) are rare. All 3×200 γ_A estimates lie within the plotted domain. The same holds for σ_{AA} , except for 13 σ_{SS} and five $\sigma_{\eta\eta}$ estimates, which satisfy $-8 \leq \log_{10}(\sigma_{AA}/A_0) \leq -6$. Similarly encouraging results are obtained for γ_Ω and are not overplotted for the sake of readability.

5. Conclusion

The accretion disk and magnetosphere of an accretion-powered pulsar form a stochastic dynamical system, driven by complicated processes such as flicker noise in the disk α parameter and self-healing Rayleigh-Taylor instabilities at the disk-magnetosphere boundary. Simultaneous, high-time-resolution measurements of the aperiodic X-ray luminosity $L(t)$ and spin period $P(t)$ can be combined to probe the disk-magnetosphere physics. Most previous, pioneering work in this direction involves temporal averaging explicitly or implicitly, e.g. when measuring and interpreting the scaling between flux and root-mean-square variability (Revnivtsev & Mereghetti 2015; Patruno & Watts 2021), the scaling between torque and luminosity (Baykal & Oegelman 1993; Sanna et al. 2017; Serim et al. 2021), and the torque and luminosity PSDs (Bildsten et al. 1997; Riggio et al. 2008; Revnivtsev et al. 2009; Patruno & Watts 2021). However the specific, time-ordered sequence of noisy measurements $L(t_n)$ and $P(t_n)$ contains a great deal of useful, additional information, such as instantaneous (anti)correlations between the system variables, which is lost after averaging over time.

In this paper, we show how to extract the instantaneous information in the stochastic time series $L(t_n)$ and $P(t_n)$ using a standard Kalman filter with the discrete-time structure set out in §3. We show that it is possible in principle to measure important accretion parameters, which cannot be disentangled by a time-averaged analysis. The Kalman filter relates $L(t_n)$ and $P(t_n)$ to three hidden state variables, which are of prime physical interest but cannot be measured directly: the mass accretion rate Q , the Maxwell stress S at the disk-magnetosphere boundary, and the radiative efficiency η . The state variables evolve according to the canonical magnetocentrifugal theory of accretion, linearized about magnetocentrifugal equilibrium, and execute mean-reverting random walks driven by white noise. Colored noise and modified forms of mean reversion fit comfortably within the formalism, if future data demand their inclusion; preliminary extensions to magnetocentrifugal disequilibrium and a generalized accretion model are outlined briefly in Appendices B and C respectively by way of illustration. The linear Kalman filter is defined completely by the dynamical equations (13) and (14), the measurement equations (15) and (16), and the equilibrium state $(\Omega_0, Q_0, S_0, \eta_0)$, which is determined from the time-averaged and Kalman filtered data assuming fiducial values of M , R , and I .

Tests on synthetic data in §4 demonstrate that the Kalman filter, combined with a nested sampler, recovers the seven model parameters $\Theta = (\gamma_\Omega, \gamma_A, \sigma_{AA})$ with $A \in \{Q, S, \eta\}$ unambiguously, confirming the formal identifiability analysis in Appendix D. It achieves an ensemble-averaged accuracy of better than ≈ 0.1 dex (absolute error in the mode) and a dispersion of less than ≈ 0.6 dex (full width half maximum) for every Θ component, assuming typical data volumes, viz. a few hundred measurements, and parameters representative of accretion-powered pulsars. Interestingly, the method estimates not just the fluctuation parameters γ_A and σ_{AA} but also the equilibrium state through γ_Ω , breaking the degeneracy that exists between Ω_0 , Q_0 , S_0 , and η_0 , when one is restricted to time-averaged data only. By doing so, the method makes it possible to measure the star’s magnetic moment μ , at least in principle, which is important physically. The tests in §4 serve as a practical, end-to-end tutorial on how to apply the method, from computing the equilibrium state to running the Kalman filter and interpreting its output.

The next step is to apply the Kalman filter to real, astronomical data in collaboration with the X-ray timing community. As just one example, it would be interesting to reanalyse the source 2S 1417–624, a bright, transient, accretion-powered pulsar (Serim et al. 2021). At the time of writing, time series of $P(t_n)$ and the pulsed X-ray flux — but not $L(t_n)$ — have been released publicly for 2S 1417–624 by the *Fermi* Gamma-Ray Burst Monitor (GBM)

Accreting Pulsars Program. ¹¹ The same source was observed independently by *NICER* during its 2018 outburst in three intervals between MJD 58211 and MJD 58350. In the *NICER* data, $L(t_n)$ is available publicly but $P(t_n)$ is not, the opposite of the situation with *Fermi*. One can generate $P(t_n)$ from public data in principle, but the timing analysis is not trivial and needs involvement from experts with custom-designed software and a thorough understanding of the systematic (e.g. calibration) uncertainties; see §4.1 in Serim et al. (2021) for details. Looking ahead to the future, it would be advantageous to release simultaneous $P(t_n)$ and $L(t_n)$ time series for every target in the *Fermi* GBM Accreting Pulsars Program. With these data, it should be possible to compile statistics about the fluctuation parameters γ_A and σ_{AA} with $A \in \{Q, S, \eta\}$ across the subset of the accreting pulsar population, where the canonical magnetocentrifugal model is thought to describe the accretion physics to a reasonable approximation.

A promising avenue for future work is gravitational wave astronomy. Spin wandering is a key limitation on searches for continuous gravitational radiation from low-mass X-ray binaries (Watts et al. 2008; Riles 2013; Mukherjee et al. 2018; Riles 2022). The coherence time T_{drift} of a search with an optimal matched filter, such as the maximum likelihood \mathcal{F} -statistic (Jaranowski et al. 1998), must be short enough, such that the quasimonochromatic signal stays inside a single Fourier bin throughout the coherent integration. That is, its root-mean-square frequency fluctuation must satisfy (Suvorova et al. 2017)

$$\langle \delta\Omega(T_{\text{drift}})^2 \rangle^{1/2} \leq \pi/T_{\text{drift}} . \quad (20)$$

In nonpulsating systems, such as the high-priority LIGO target Scorpius X–1, where $\Omega(t)$ cannot be measured directly, one is obliged to guess T_{drift} by analogy from the PSD of $L(t)$; a popular choice is $T_{\text{drift}} \sim 10$ days for Scorpius X–1 (Mukherjee et al. 2018). An improved theoretical understanding of the connection between $\Omega(t)$ and $L(t)$ in magnetocentrifugal accretion, facilitated by the Kalman filter in this paper, would help refine PSD-based estimates of T_{drift} . Indeed, it may even be possible to estimate directly a subset of the parameters Θ with a Kalman filter from the time series $L(t_n)$ alone, as in other neutron star applications where observations are incomplete (Meyers et al. 2021); see also Meyers et al. (2021). Specifically, if it is possible to estimate γ_Ω , γ_Q , γ_S , σ_{QQ} , and σ_{SS} from $L(t_n)$, one can solve the inequality (20) for the maximum T_{drift} by substituting (D6) into the left-hand side of (20). We will explore this opportunity in a forthcoming paper.

The authors thank Katie Auchettl for discussions about X-ray observations of accretion-powered pulsars. We are also grateful to the anonymous referee for specific feedback and

¹¹<https://gammaray.msfc.nasa.gov/gbm/science/pulsars.html>

concrete suggestions about the idealizations in the accretion physics, which clarified several important points and inspired the calculations in Appendices B and C. This research was supported by the Australian Research Council Centre of Excellence for Gravitational Wave Discovery (OzGrav), grant number CE170100004. NJO’N is the recipient of a Melbourne Research Scholarship.

REFERENCES

- Andersson N., Glampedakis K., Haskell B., Watts A. L., 2005, *MNRAS*, 361, 1153
- Baykal A., 1997, *A&A*, 319, 515
- Baykal A., Alpar A., Kiziloglu U., 1991, *A&A*, 252, 664
- Baykal A., Oegelman H., 1993, *A&A*, 267, 119
- Bellman R., Åström K. J., 1970, *Mathematical Biosciences*, 7, 329
- Bildsten L., 1998, *ApJ*, 501, L89
- Bildsten L., Chakrabarty D., Chiu J., Finger M. H., Koh D. T., Nelson R. W., Prince T. A., Rubin B. C., Scott D. M., Stollberg M., Vaughan B. A., Wilson C. A., Wilson R. B., 1997, *ApJS*, 113, 367
- Blandford R. D., Payne D. G., 1982, *MNRAS*, 199, 883
- Campana S., Gastaldello F., Stella L., Israel G. L., Colpi M., Pizzolato F., Orlandini M., Dal Fiume D., 2001, *ApJ*, 561, 924
- Chashkina A., Lipunova G., Abolmasov P., Poutanen J., 2019, *A&A*, 626, A18
- D’Angelo C. R., 2017, *MNRAS*, 470, 3316
- D’Angelo C. R., Spruit H. C., 2010, *MNRAS*, 406, 1208
- D’Angelo C. R., Spruit H. C., 2012, *MNRAS*, 420, 416
- Das P., Porth O., Watts A. L., 2022, *MNRAS*
- de Kool M., Anzer U., 1993, *MNRAS*, 262, 726
- De Marco B., Motta S. E., Belloni T. M., 2022, arXiv e-prints, p. arXiv:2209.13467
- Elorrieta F., Eyheramendy S., Palma W., Ojeda C., 2021, *MNRAS*, 505, 1105

- Foucart F., Lai D., 2011, MNRAS, 412, 2799
- Gardiner C. W., 1994, Handbook of stochastic methods for physics, chemistry and the natural sciences. Springer Series in Synergetics, Berlin: Springer, —c1994, 2nd ed. 1985. Corr. 3rd printing 1994
- Gelb A., 1974, Applied Optimal Estimation. MIT Press
- Gençali A. A., Niang N., Toyran O., Ertan Ü., Ulubay A., Şaşmaz S., Devlen E., Vahdat A., Özcan Ş., Alpar M. A., 2022, A&A, 658, A13
- Gendreau K. C., Arzoumanian Z., Adkins P. W., Albert C. L., Anders J. F., Aylward A. T., Baker C. L., Balsamo E. R., Bamford W. A., Benegalrao S. S., et. al. 2016, in den Herder J.-W. A., Takahashi T., Bautz M., eds, Space Telescopes and Instrumentation 2016: Ultraviolet to Gamma Ray Vol. 9905 of Society of Photo-Optical Instrumentation Engineers (SPIE) Conference Series, The Neutron star Interior Composition Explorer (NICER): design and development. p. 99051H
- Ghosh P., Lamb F. K., 1979, ApJ, 234, 296
- Goetz E., Riles K., 2011, Classical and Quantum Gravity, 28, 215006
- González-Galán A., Kuulkers E., Kretschmar P., Larsson S., Postnov K., Kochetkova A., Finger M. H., 2012, A&A, 537, A66
- Haskell B., Priymak M., Patruno A., Oppenoorth M., Melatos A., Lasky P. D., 2015, MNRAS, 450, 2393
- Hu Z., Tak H., 2020, AJ, 160, 265
- Ireland L. G., Matt S. P., Zanni C., 2022, ApJ, 929, 65
- Jaranowski P., Królak A., Schutz B. F., 1998, Phys. Rev. D, 58, 063001
- Jazwinski A. H., 1970, Stochastic Processes and Filtering Theory. Academic Press
- Julier S. J., Uhlmann J. K., 1997, in Kadar I., ed., Signal Processing, Sensor Fusion, and Target Recognition VI Vol. 3068 of Society of Photo-Optical Instrumentation Engineers (SPIE) Conference Series, New extension of the Kalman filter to nonlinear systems. pp 182–193
- Kalman R. E., 1960, Transactions of the ASME: Journal of Basic Engineering, 82, 35
- Kelly B. C., Becker A. C., Sobolewska M., Siemiginowska A., Uttley P., 2014, ApJ, 788, 33

- Klus H., Ho W. C. G., Coe M. J., Corbet R. H. D., Townsend L. J., 2014, MNRAS, 437, 3863
- Kulkarni A. K., Romanova M. M., 2008, MNRAS, 386, 673
- Lai D., 2014, in European Physical Journal Web of Conferences Vol. 64 of European Physical Journal Web of Conferences, Theory of Disk Accretion onto Magnetic Stars. p. 01001
- Lazzati D., Stella L., 1997, ApJ, 476, 267
- Locsei J. T., Melatos A., 2004, MNRAS, 354, 591
- Lyubarskii Y. E., 1997, MNRAS, 292, 679
- Mannattil M., Gupta H., Chakraborty S., 2016, ApJ, 833, 208
- Marino A., Di Salvo T., Burderi L., Sanna A., Riggio A., Papitto A., Del Santo M., Gambino A. F., Iaria R., Mazzola S. M., 2019, A&A, 627, A125
- Matt S., Pudritz R. E., 2005, ApJ, 632, L135
- Matt S., Pudritz R. E., 2008, ApJ, 681, 391
- Melatos A., Clearwater P., Suvorova S., Sun L., Moran W., Evans R. J., 2021, Phys. Rev. D, 104, 042003
- Melatos A., Mastrano A., 2016, ApJ, 818, 49
- Melatos A., Payne D. J. B., 2005, ApJ, 623, 1044
- Meyers P. M., Melatos A., O’Neill N. J., 2021, MNRAS, 502, 3113
- Meyers P. M., O’Neill N. J., Melatos A., Evans R. J., 2021, MNRAS, 506, 3349
- Middleton H., Clearwater P., Melatos A., Dunn L., 2020, Phys. Rev. D, 102, 023006
- Mönkkönen J., Tsygankov S. S., Mushtukov A. A., Doroshenko V., Suleimanov V. F., Poutanen J., 2022, MNRAS
- Mukherjee A., Messenger C., Riles K., 2018, Phys. Rev. D, 97, 043016
- Mushtukov A., Tsygankov S., 2022, arXiv e-prints, p. arXiv:2204.14185
- Nelson R. W., Bildsten L., Chakrabarty D., Finger M. H., Koh D. T., Prince T. A., Rubin B. C., Scott D. M., Vaughan B. A., Wilson R. B., 1997, ApJ, 488, L117

- Papitto A., Riggio A., Burderi L., di Salvo T., D’Aí A., Iaria R., 2011, *A&A*, 528, A55
- Papitto A., Torres D. F., 2015, *ApJ*, 807, 33
- Patruno A., 2010, *ApJ*, 722, 909
- Patruno A., 2012, *ApJ*, 753, L12
- Patruno A., Watts A. L., 2021, *Astrophysics and Space Science Library*, 461, 143
- Patruno A., Wijnands R., van der Klis M., 2009, *ApJ*, 698, L60
- Payne D. J. B., Melatos A., 2004, *MNRAS*, 351, 569
- Priymak M., Melatos A., Payne D. J. B., 2011, *MNRAS*, 417, 2696
- Revnivtsev M., Churazov E., Postnov K., Tsygankov S., 2009, *A&A*, 507, 1211
- Revnivtsev M., Mereghetti S., 2015, *Space Sci. Rev.*, 191, 293
- Riggio A., Di Salvo T., Burderi L., Menna M. T., Papitto A., Iaria R., Lavagetto G., 2008, *ApJ*, 678, 1273
- Riles K., 2013, *Progress in Particle and Nuclear Physics*, 68, 1
- Riles K., 2022, arXiv e-prints, p. arXiv:2206.06447
- Romanova M. M., Koldoba A. V., Ustyugova G. V., Blinova A. A., Lai D., Lovelace R. V. E., 2021, *MNRAS*, 506, 372
- Romanova M. M., Owocki S. P., 2015, *Space Sci. Rev.*, 191, 339
- Romanova M. M., Ustyugova G. V., Koldoba A. V., Lovelace R. V. E., 2005, *ApJ*, 635, L165
- Romanova M. M., Ustyugova G. V., Koldoba A. V., Lovelace R. V. E., 2009, *MNRAS*, 399, 1802
- Romanova M. M., Ustyugova G. V., Koldoba A. V., Wick J. V., Lovelace R. V. E., 2003, *ApJ*, 595, 1009
- Rößler A., 2010, *SIAM Journal on Numerical Analysis*, 48, 922
- Sanna A., Riggio A., Burderi L., Pintore F., Di Salvo T., D’Aí A., Bozzo E., Esposito P., Segreto A., Scarano F., Iaria R., Gambino A. F., 2017, *MNRAS*, 469, 2
- Scaringi S., Maccarone T. J., Middleton M., 2014, *MNRAS*, 445, 1031

- Serim D., Serim M. M., Baykal A., 2022, arXiv e-prints, p. arXiv:2207.00248
- Serim M. M., Ozudogru O. C., Donmez C. K., Sahiner S., Serim D., Baykal A., Inam S. C., 2021, arXiv e-prints, p. arXiv:2107.14492
- Shibazaki N., Murakami T., Shaham J., Nomoto K., 1989, *Nature*, 342, 656
- Speagle J. S., 2020, *MNRAS*, 493, 3132
- Spruit H. C., Taam R. E., 1993, *ApJ*, 402, 593
- Suvorova S., Clearwater P., Melatos A., Sun L., Moran W., Evans R. J., 2017, *Phys. Rev. D*, 96, 102006
- The LIGO Scientific Collaboration, the Virgo Collaboration, the KAGRA Collaboration, et al. 2021, arXiv e-prints, p. arXiv:2109.09255
- Timmer J., Schwarz U., Voss H. U., Wardinski I., Belloni T., Hasinger G., van der Klis M., Kurths J., 2000, *Phys. Rev. E*, 61, 1342
- Uttley P., McHardy I. M., 2001, *MNRAS*, 323, L26
- Uzdensky D. A., 2004, *Ap&SS*, 292, 573
- van Kerkwijk M. H., Chakrabarty D., Pringle J. E., Wijers R. A. M. J., 1998, *ApJ*, 499, L27
- Wang J., Zhang C. M., Zhao Y. H., Kojima Y., Yin H. X., Song L. M., 2011, *A&A*, 526, A88
- Wang Y. M., 1987, *A&A*, 183, 257
- Watts A. L., Krishnan B., Bildsten L., Schutz B. F., 2008, *MNRAS*, 389, 839
- Whelan J. T., Sundaesan S., Zhang Y., Peiris P., 2015, *Phys. Rev. D*, 91, 102005
- Yan Z., Yu W., 2015, *ApJ*, 805, 87
- Yang J., Laycock S. G. T., Christodoulou D. M., Fingerman S., Coe M. J., Drake J. J., 2017, *ApJ*, 839, 119
- Zanni C., Ferreira J., 2013, *A&A*, 550, A99
- Zhang C. M., Kojima Y., 2006, *MNRAS*, 366, 137

A. Equilibrium state vector in terms of observables

The magnetocentrifugal equilibrium defined in §2.3 is described by the state vector $(\Omega_0, Q_0, S_0, \eta_0)$, whose four components are formal inputs into the Kalman filter in §3. In this appendix it is shown how to solve for $(\Omega_0, Q_0, S_0, \eta_0)$ following approaches I and II introduced in §2.3, which use time-averaged and Kalman filtered data respectively. In what follows, we assume that M , R , and I are known *a priori* on theoretical grounds. They occur in inseparable combinations and cannot be inferred uniquely from the data.

Upon averaging the measurements $P(t_n)$ and $L(t_n)$ over time, and combining with the condition for magnetocentrifugal equilibrium, we obtain three pieces of independent information about $(\Omega_0, Q_0, S_0, \eta_0)$. From the definitions of Ω_0 and L_0 in §2.3, we have

$$\Omega_0 = N^{-1} \sum_{n=1}^N 2\pi/P(t_n) \quad (\text{A1})$$

and

$$L_0 = N^{-1} \sum_{n=1}^N L(t_n) . \quad (\text{A2})$$

Equation (A1) gives Ω_0 directly. Secondly, combining (A1) with the zero-torque condition (6) implies a relation between Q_0 and S_0 . Thirdly, combining (A2) with the energy conservation law (7) implies a relation between Q_0 and η_0 . The sample means (A1) and (A2) do not equate exactly to the true equilibrium values of the dynamical variables $\Omega(t)$ and $L(t)$ in (6) and (7) due to random dispersion of fractional order $N^{-1/2}$ and systematic errors if the accretion physics is not stationary. However, there is no realistic alternative to using the sample means; it is a standard approach when interpreting data in terms of the magnetocentrifugal accretion paradigm (Patruno & Watts 2021).

The two relations between Q_0 , S_0 and η_0 obtained from (6) and (7), using the data in (A1) and (A2), must be supplemented by another piece of information to solve for Q_0 , S_0 and η_0 uniquely. Approach I in §2.3 involves assuming a plausible value for one unknown, solving for the other two, and running the Kalman filter in §3 with all four components of $(\Omega_0, Q_0, S_0, \eta_0)$ fixed. It is natural but not obligatory to assume η_0 , which is bounded ($0 < \eta_0 < 1$) and widely believed to satisfy $\eta_0 \sim 1$ (Bildsten et al. 1997; Sanna et al. 2017).

Approach II in §2.3 is more general: it keeps one component of $(\Omega_0, Q_0, S_0, \eta_0)$ free to be estimated. Specifically, the linearized equations of motion (13) feature the parameter $\gamma_\Omega[\Omega_0, Q_0, R_{\text{m0}}(\Omega_0)]$ defined by (14), viz.

$$\gamma_\Omega = \frac{(GM)^{2/3} Q_0}{I \Omega_0^{4/3}} , \quad (\text{A3})$$

where (A3) follows from (14) and $R_{m0} = R_{c0} = (GM)^{1/3}\Omega_0^{-2/3}$. Approach II involves running the parameter estimation scheme with γ_Ω free, so that it is one of the parameters estimated from the data. This yields a relation between Ω_0 and Q_0 , which is combined with (A1) and the relations derived from (6) and (7) to solve for all four components of $(\Omega_0, Q_0, S_0, \eta_0)$. Handy formulas are quoted below for the convenience of the reader:

$$Q_0 = \frac{I\Omega_0^{4/3}\gamma_\Omega}{(GM)^{2/3}}, \quad (\text{A4})$$

$$S_0 = \frac{I\Omega_0^3\gamma_\Omega}{4\pi GM}, \quad (\text{A5})$$

$$\eta_0 = \frac{RL_0}{(GM)^{1/3}I\Omega_0^{4/3}\gamma_\Omega}. \quad (\text{A6})$$

We reiterate that M , R , and I cannot be inferred uniquely from the data; fiducial values are inserted instead.

B. Magnetocentrifugal disequilibrium

B.1. Intervals of secular acceleration and deceleration

Many accretion-powered pulsars exist well away from the state of magnetocentrifugal equilibrium, satisfying $|R_c(t) - R_m(t)| \gtrsim R_c(t)$ for example (Bildsten et al. 1997; Yang et al. 2017; Mushtukov & Tsygankov 2022; Serim et al. 2022). Disequilibrium occurs in low-mass X-ray binaries, such as Her X–1 and 4U 1626–67, which accrete via a persistent disk fed by Roche lobe overflow (Gençali et al. 2022); symbiotic X-ray binaries, such as GX 1+4, which may involve quasispherical accretion (González-Galán et al. 2012); and high-mass X-ray binaries, such as GX 301–2, 4U 1538–52, OAO 1657–415, Vela X–1, and Cen X–3, which accrete via a transient disk fed by a supergiant wind (and possibly Roche lobe overflow too) (Serim et al. 2022). In disequilibrium, the star alternates between long spin-up and spin-down episodes, which last for $\gtrsim 10$ yr, separated by fast transitions lasting as short as ~ 1 day, e.g. in 4U 0115+63 (Campana et al. 2001); see Figures 6 and 31 in Bildsten et al. (1997), Figure 19 in Mushtukov & Tsygankov (2022), and Figures 1–7 in Serim et al. (2022) for typical examples. Sometimes, as in A 0535+26, X-ray outbursts and quiescence are correlated with acceleration and deceleration episodes respectively; see Figure 19 in Mushtukov & Tsygankov (2022).

The Kalman filter technique introduced in this paper is new in the context of parameter estimation for accretion-powered pulsars. It is prudent, therefore, to validate it first with objects that are near magnetocentrifugal equilibrium, where the linear theory in §2.5 and

linear Kalman filter in §3 apply without modification, before attempting the more ambitious application to disequilibrium. Real data exist on many objects near equilibrium, e.g. 30 out of the 65 known X-ray pulsars in the Small Magellanic Cloud, labeled by the letter ‘C’ in Table 3 in Yang et al. (2017), whose time-averaged dP/dt values are smaller than 1.5 times the measurement error on dP/dt .

It is straightforward in principle to generalize the analysis in §2 and §3 to objects in disequilibrium, by analyzing the spin-up and spin-down intervals separately. An advantage in doing so is that one can compare and gain physical insight from the parameter values estimated independently from consecutive intervals. Some parameters (e.g. η_0 , if dominated by radiative processes) may be expected to remain roughly unchanged, whereas others (e.g. Q_0 , if driven by the companion star’s mass loss rate) may change substantially. Another advantage is that an interval-by-interval analysis does not rely on modifying (5) and (9)–(11) to track the fast torque transition, which is not understood fully yet in terms of simple analytic laws like (5) and (9)–(11), which are needed to implement a Kalman filter (Nelson et al. 1997; van Kerkwijk et al. 1998; Locsei & Melatos 2004; Lai 2014; Gençali et al. 2022). The torque transition is related to the challenging physics of the disk-magnetosphere boundary, which is surveyed briefly in Appendix C.

B.2. Worked example: unscented Kalman filter applied to a secular interval

We present for the sake of completeness a short worked example to illustrate how a simple, nonlinear adjustment of the framework in §2 can be made to analyze an individual spin-up or spin-down interval satisfying $R_c(t) \neq R_m(t)$. The adjustment proceeds in two steps. First, we replace the linearized measurement equations (15) and (16) with their nonlinear counterparts (1) and (2) respectively. Second, we replace the linearized equations of motion (13) and (14) with the nonlinear torque law (5) and new Langevin equations,

$$\frac{dQ}{dt} = -\gamma_Q[Q(t) - \bar{Q}] + \xi_Q(t) , \tag{B1}$$

$$\frac{dS}{dt} = -\gamma_S[S(t) - \bar{S}] + \xi_S(t) , \tag{B2}$$

$$\frac{d\eta}{dt} = -\gamma_\eta[\eta(t) - \bar{\eta}] + \xi_\eta(t) . \tag{B3}$$

Equations (B1)–(B3) describe linear mean reversion in common with (9)–(11); see Appendix C for some of the refinements required to make the mean reversion more realistic physically through nonlinear feedback. Indeed, equations (B1)–(B3) are identical mathematically to (9)–(11). However, they are interpreted differently. For example, $\bar{Q} = \langle Q(t) \rangle$ in (B1), the

ensemble average of $Q(t)$, replaces the equilibrium quantity Q_0 in (9). Taking $\bar{Q} > Q_0$, we have $\bar{R}_m = \langle R_m(t) \rangle < R_c$ and hence $d\Omega/dt > 0$ on average; the magnetosphere is compressed relative to equilibrium. In contrast, $\bar{Q} < Q_0$ implies $d\Omega/dt < 0$, i.e. the propeller phase. Here \bar{Q} is a static parameter to be estimated by the Kalman filter.

Kalman parameter estimation for nonlinear problems, such as (1), (2), (5), and (B1)–(B3), is a standard procedure. Algorithms include the extended and unscented Kalman filters (Jazwinski 1970; Julier & Uhlmann 1997). In the worked example in this appendix, we use an unscented Kalman filter, which shares the same predictor-corrector design as the linear Kalman filter. It works on the principle that a set of weighted sampling points (‘sigma points’), generated deterministically from the matrix square root of the state covariance matrix, are used to estimate the mean and covariance of the conditional probability density. The algorithm is laid out in standard textbooks and in Box 3.1 of the original paper by Julier & Uhlmann (1997). The Kalman log-likelihood is given by (17) and evaluated by the **dynesty** nested sampler (Speagle 2020).¹² The parameters to be estimated are $\Theta = (\beta_1, \beta_2, \gamma_A, \sigma_{AA})$, with

$$\beta_1 = \frac{(GM)^{3/5} \bar{Q}^{6/5}}{(4\pi)^{1/5} I \bar{S}^{1/5} \bar{\Omega}}, \quad (\text{B4})$$

$$\beta_2 = \frac{(GM)^{2/5} \bar{Q}^{9/5}}{(4\pi)^{4/5} I \bar{S}^{4/5}}, \quad (\text{B5})$$

and $A \in \{Q, S, \eta\}$, i.e. eight parameters instead of the seven in the linearized recipe in §3. In (B4), $\bar{\Omega} = \langle \Omega(t) \rangle$ is obtained directly from the data by calculating the sample average (A1) without assuming an attendant equilibrium interpretation. Once $\Theta = (\beta_1, \beta_2, \gamma_A, \sigma_{AA})$ is estimated, we solve (B4) and (B5) for \bar{Q} and \bar{S} and then solve

$$\bar{L} = GM \bar{Q} \bar{\eta} / R \quad (\text{B6})$$

for $\bar{\eta}$, where $\bar{L} = \langle L(t) \rangle$ is obtained directly from the data by calculating the sample average (A2), again without assuming equilibrium. In this appendix, for the sake of simplicity, we assume that $\bar{Q} \bar{\eta}$ reduces to \bar{Q} times $\bar{\eta}$, as we do not estimate $\bar{\eta}$ in the worked example below. In general, however, $Q(t)$ and $\eta(t)$ are correlated, and

$$\beta_3 = \frac{\langle Q(t) \eta(t) \rangle}{\langle Q(t) \rangle \langle \eta(t) \rangle} \quad (\text{B7})$$

represents a ninth parameter to be appended to Θ and estimated.

¹²In an unscented Kalman filter, $\mathbf{s}_n = \langle \mathbf{e}_n \mathbf{e}_n^T \rangle$ in (17) is often called the predicted measurement covariance and is calculated as a weighted average over the sigma points (Julier & Uhlmann 1997).

Figure 4 displays the tracking and estimation results for a hypothetical pulsar in disequilibrium. Its injected parameters are the same as in Table 1, but we take $\bar{Q} = 2Q_0$ in (B1), so that the pulsar spins up secularly throughout the observation. (Secular spin down, e.g. $\bar{Q} = 0.5Q_0$, works the same way.) We also take $\bar{S} = 2^{12/7}S_0$ in (B2) to keep $\mu \propto \bar{S}^{-7/10}\bar{Q}^{6/5}$ unchanged relative to Table 1. One sees clearly the expected downward trend in the synthetic measurements of $P(t_n)$ in the top panel on the left, and the upward trend in the tracked state variable $\Omega(t_n)$ in the third panel on the left. One also sees $Q(t)$ executing mean-reverting fluctuations around \bar{Q} in the fourth panel on the left, in line with (B1). By inspection, the Kalman state estimates (colored curves) track the injected state sequence (black, dashed curves) accurately. The synthetic measurements of $L(t_n)$ resemble qualitatively those in Figure 1, as do the Kalman state estimates of $S(t)$ and $\eta(t)$ (not plotted for clarity).

The right panel of Figure 4 displays the posterior distribution (corner plot) of \bar{Q} and \bar{S} , inferred from β_1 and β_2 via (B4) and (B5) and marginalized over (γ_A, σ_{AA}) with $A \in \{Q, S, \eta\}$. Priors are uniform and run from 0.1 to 10 times the injected value per parameter. The peak coincides with the injected values to within ≈ 0.080 dex and ≈ 0.034 dex for \bar{Q} and \bar{S} respectively. The uncertainty (full width half maximum) amounts to ≈ 0.021 dex and ≈ 0.011 dex for \bar{Q} and \bar{S} respectively. Encouragingly, the error in the peak and the full width half maximum are small, in the sense that both sit well inside the prior range (± 1 dex). The corner plot shows that the peak is biased marginally yet systematically away from the injected values, in the sense that the error in the peak exceeds the full width half maximum (exaggerated visually in the right panel of Figure 4 by the fine horizontal scale). Such a bias, although negligible in practice, is typical of certain nonlinear estimation algorithms (Gelb 1974); cf. the unbiased results of the linear Kalman filter in Figure 2. Its smallness engenders confidence in the approximations involved, e.g. $\beta_3 = 0$. Overall, the results in Figure 4 are comparable to Figures 1 and 2.

C. Refining the description of the disk-magnetosphere boundary

The accretion physics analyzed in this paper is presented deliberately in a simple form, which adheres to the canonical magnetocentrifugal picture introduced by Ghosh & Lamb (1979) and applied widely since (Patruno & Watts 2021). There are three motivations for this approach. (i) It is the first time in the literature that a Kalman filter is applied to estimate the parameters of accretion-powered pulsars, so it is prudent to present the statistical technique simply for clarity. (ii) Data sets available now and in the foreseeable future are limited to $N \lesssim 10^3$ samples $P(t_n)$ and $L(t_n)$. It is asking a lot of a Kalman filter to estimate more parameters

than the seven in §3.1, despite the encouraging test results in Figures 1–3 and §4. (iii) There is no consensus in the literature about how to refine the canonical magnetocentrifugal model through simple analytic modifications. Impressive progress is occurring through three-dimensional magnetohydrodynamic simulations (Romanova & Owocki 2015), but the output of such simulations does not take a form that feeds easily into a Kalman filter or equivalent parameter estimation scheme.

That said, we emphasize that aspects of the fluctuation dynamics in accretion-powered pulsars may not be represented accurately by the white-noise, mean-reverting Langevin equations (5) and (9)–(11). Data available today may not suffice to expose the inaccuracies, as noted above, but it is important to start investigating them in principle, in anticipation of more data in the future. In this appendix, we take a preliminary first step towards refining the accretion model, by adding deterministic descriptions of some of the complicated variability at the disk-magnetosphere boundary, which is absorbed in the Langevin dynamics in the main text. We draw heavily on the theory of episodic accretion and trapped disks (D’Angelo & Spruit 2010, 2012; D’Angelo 2017) by way of illustration, and because it proposes convenient and soundly motivated analytic scalings, without seeking to privilege it over plausible and complementary alternatives in the literature; see Lai (2014) for a review.

C.1. Complexities at the boundary

The central approximation in (5) and (9)–(11) is that there exists a sharp boundary at radius $r = R_m$ between a corotating dipole magnetosphere at $r < R_m$ and a thin accretion disk at $r > R_m$. In reality, the transition from magnetosphere to disk occurs gradually, over an interaction region $R_m - \Delta R \leq r \leq R_m$, with the disk surface density vanishing at $R_{\text{in}} = R_m - \Delta R$ (D’Angelo & Spruit 2010). This has implications for the hidden variables $Q(t)$, $S(t)$, and $\eta(t)$. (i) In the interaction region, the accretion flow is sheared and variable, and the toroidal and vertical magnetic field components penetrating the region, viz. B_ϕ and B_z respectively, where (r, ϕ, z) are cylindrical polar coordinates, fluctuate in a complicated manner in space and time. The scalar Maxwell stress $S(t)$ is inadequate by itself to capture the physics; the ratio $\eta_B = |B_\phi/B_z| \lesssim 1$ also plays an important role at the next level of approximation (Wang 1987; Spruit & Taam 1993). (ii) Vertical forces act to squeeze or inflate the disk, to the point where it is not always thin. For example, the disk magnetic pressure $\sim B_\phi^2/(8\pi)$ can launch a vertical outflow, opening up magnetic field lines and disconnecting the disk at $r \gtrsim R_m$ magnetically from the star (before possibly reconnecting). This modifies (10) for $S(t)$. (iii) Radial forces in the interaction region decelerate the infall and shut it off completely in the propeller regime $R_m \gg R_c$, an effect which is absent from (11), which

maintains $\eta(t) \approx \eta_0$ for all t irrespective of R_m/R_c . The transition from free fall to propeller occurs abruptly over a transition length scale $\Delta R_2 \sim \Delta R$, with $|R_m - R_c| \lesssim \Delta R_2$ and $\Delta R_2 \neq \Delta R$ in general (D’Angelo & Spruit 2010). (iv) In the regime $R_c < R_m \lesssim 1.3R_c$, the disk-magnetosphere interaction may deposit enough angular momentum in the interaction region to pause the infall, so that gas piles up near R_m without unbinding gravitationally before it breaks through and accretes episodically onto the star, viz. the trapped disk phenomenon (D’Angelo & Spruit 2010, 2012; D’Angelo 2017). (v) If enough energy and angular momentum are deposited in the interaction region, parts of the disk at $r \gtrsim R_m$ unbind, launching a vertical outflow along twisted magnetic field lines (Matt & Pudritz 2005; Romanova & Owocki 2015). An outflow modifies (9) for $Q(t)$. All the phenomena (i)–(v) are observed in three-dimensional magnetohydrodynamic simulations (Romanova & Owocki 2015).

In what follows, we investigate two rudimentary modifications of (5) and (9)–(11), as a starting point for assessing the impact of the above phenomena on the Kalman filter framework. In Appendix C.2, we extend the torque and mass transfer laws (5) and (11) to include abrupt switching from the infall to the propeller regimes, following the “hyperbolic tangent” approximation in D’Angelo (2017). Kalman filter results are generated for representative values of ΔR_2 . In Appendix C.3, we analyze the trapped disk scenario in D’Angelo & Spruit (2010) approximately by modifying the definition (3) for R_m (Spruit & Taam 1993), adding a ΔR_2 -dependent transition to $\eta(t)$ via (11), and adding a ΔR -dependent term to the torque via (5) following D’Angelo & Spruit (2012), without solving self-consistently for the disk surface mass density [cf. D’Angelo & Spruit (2010, 2012)], which is outside the scope of this paper and burdens the Kalman filter with too many parameters to estimate. Kalman filter results are generated for representative values of ΔR and ΔR_2 . Finally, in Appendix C.4, we summarize qualitatively some of the issues raised by disk and stellar outflows but do not model them mathematically, as they lie outside the scope of the paper and the Kalman filter’s capacity at present, and analytic prescriptions like those in Appendices C.2 and C.3 are hard to develop.

C.2. Propeller transition

As a starting point in modifying (5) and (9)–(11), we incorporate approximately two aspects of the propeller transition. First, we replace (5) with

$$\frac{d\Omega}{dt} = I^{-1}(GM)^{1/2}R_m(t)^{1/2}Q(t) \tanh \left[\frac{R_c(t) - R_m(t)}{\Delta R_2} \right], \quad (\text{C1})$$

which matches equation (3) in D’Angelo (2017) up to a dimensionless proportionality constant of order unity, which cannot be estimated independently by the Kalman filter and

is absorbed into $I^{-1}(GM)^{1/2}$. The definitions (3) and (4) of $R_m(t)$ and $R_c(t)$ respectively remain unchanged. Equation (C1) describes the same sign change in the torque as (5), from $d\Omega/dt > 0$ for $R_m < R_c$ to $d\Omega/dt < 0$ for $R_m > R_c$, but it allows the sign change to occur more abruptly, if one has $\Delta R_2 \ll R_c$. The transition length scale ΔR_2 is added to the parameter set Θ , which the Kalman filter estimates.

Second, we replace the stochastic Langevin equation (11) with the deterministic algebraic equation

$$\eta(t) = \frac{\eta_0}{2} \left\{ 1 - \tanh \left[\frac{R_m(t) - R_c(t)}{\Delta R_2} \right] \right\}. \quad (\text{C2})$$

Equation (C2) ensures that the accretion onto the star and its associated X-ray emission switch off in the strong propeller regime $R_m \gg R_c$. This is more realistic than (11), where X-ray emission persists undiminished even for $R_m \gg R_c$, with $|\eta(t) - \eta_0| \lesssim \gamma_\eta^{-1/2} \sigma_{\eta\eta} \neq 0$. Observations show that weakly magnetized low-mass X-ray binaries and strongly magnetized Be X-ray binaries have duty cycles $\lesssim 3\%$ and $\lesssim 20\%$ respectively, and $L(t)$ varies by $\lesssim 5$ orders of magnitude between outbursts and quiescence (Klus et al. 2014; Yan & Yu 2015; D’Angelo 2017). In writing (C2) instead of (11), we assume implicitly that fluctuations in $\eta(t)$ and hence $L(t)$ are driven solely by the propeller dynamics at the disk-magnetosphere boundary. In reality, other radiative processes influence $\eta(t)$ independently of mass transfer. We do not include them in (C2) for two reasons. One, the available X-ray data do not suffice to constrain more complicated models with additional, radiative parameters. Two, the radiative processes are not described by simple analytic expressions like (C2), which is why we resort to phenomenological mean reversion in (11). Retaining (11) but replacing η_0 in (11) with the right-hand side of (C2) would be problematic, because white-noise fluctuations in (11) would send $\eta(t)$ negative for $R_m \gg R_c$, when the right-hand side of (C2) vanishes.

Figure 5 displays results from a repeat of the numerical experiment in Figures 1 and 2 and Table 1, except with (5) and (11) replaced by (C1) and (C2) respectively, and (9) and (10) replaced by (B1) and (B2) respectively. The revised model features seven parameters to be estimated, viz. $\Theta = (\beta_1, \beta_4, \beta_5, \gamma_Q, \gamma_S, \sigma_{QQ}, \sigma_{SS})$, with

$$\beta_4 = \frac{(GM)^{1/3}}{\bar{\Omega}^{2/3} \Delta R_2}, \quad (\text{C3})$$

$$\beta_5 = \frac{(GM)^{1/5} \bar{Q}^{2/5}}{(4\pi)^{2/5} \bar{S}^{2/5} \Delta R_2}, \quad (\text{C4})$$

β_1 defined according to (B4), and $\bar{\Omega}$ calculated directly from the data via the sample aver-

age (A1) without assuming an equilibrium interpretation (see Appendix B).¹³ We employ an unscented Kalman filter to analyze the nonlinear system, as in Appendix B (Julier & Uhlmann 1997), with $N = 5 \times 10^2$. We find that the Kalman filter tracks $\Omega(t)$ and $\eta(t)$ accurately; compare the colored and dashed curves in the third and fourth panels on the left of Figure 5. Likewise, $Q(t)$ and $S(t)$ are tracked accurately; they behave like in Figure 1 (or equivalently Figure 4) and are not displayed for brevity. The system undergoes several propeller transitions, e.g. from spin up to spin down at $t \approx 8 \times 10^7$ s, with $\Delta R_2 = 0.09 R_{m0}$. During the subsequent spin-down episode $0.8 \lesssim t/(10^8 \text{ s}) \lesssim 1.2$, we find $\eta(t) < \eta_0$ and hence $L(t) < \bar{L} = \langle L(t) \rangle$, as marked by dips in the fourth and second panels respectively on the left of Figure 5. Parameter estimation results are displayed in the right panel of Figure 5, where we plot the posterior for ΔR_2 , marginalized over the other six parameters (which are taken as known artificially for the purpose of this test to accelerate the computation). The error in the peak and the uncertainty (full width half maximum) are given by ≈ 0.0067 dex and ≈ 0.025 dex respectively. A preliminary analysis indicates that $N \geq 2 \times 10^3$ samples are needed to achieve convergence when scanning the complete parameter space, above what is available typically from the current generation of X-ray timing experiments. A full study of the estimation accuracy is postponed, until larger volumes of astronomical data justify the revisions (C1) and (C2).

In this section, we keep (B1) to describe mean-reverting fluctuations in the mass accretion rate driven by processes in the outer disk and companion star (Lyubarskii 1997), noting that (B1) does not incorporate outflows; see Appendix C.4. We also keep (B2) for simplicity, while noting that it is not self-consistent with (C2) and should involve more than one tensor component in general.

C.3. Disk trapping

As a next step in modifying (5) and (9)–(11), we incorporate approximately the important phenomenon of disk trapping (D’Angelo & Spruit 2010, 2012; D’Angelo 2017). In the weak propeller regime, with $R_c < R_m \lesssim 1.3 R_c$, the complex disk-magnetosphere interaction deposits enough angular momentum in the inner disk to inhibit accretion but not enough to unbind the disk material gravitationally and drive a vertical outflow, cf. Matt & Pudritz (2005). Instead, $R_m(t)$ stalls and becomes almost independent of $Q(t)$, so that the traditional

¹³Once the seven components of Θ are estimated, we can solve (B4), (C3), and (C4) for \bar{Q} , \bar{S} , and ΔR_2 , given $\bar{\Omega}$ from the data. We can then calculate $\bar{L} = \langle L(t) \rangle$ directly from the data via (A2) and solve (B6) for $\eta_0 = 2\bar{\eta}$. Correlations between $Q(t)$ and $\eta(t)$ should be treated with caution. In general, they introduce an extra parameter to be estimated, as discussed in Appendix B.2; see (B7).

magnetocentrifugal expression (3) for $R_m(t)$ is modified (Wang 1987; Spruit & Taam 1993). Gas piles up at the inner edge of the disk, changing the disk density structure near R_c and hence the torque (5). The accumulated gas eventually breaks through the magnetocentrifugal barrier, e.g. via the Rayleigh-Taylor instability, so that accretion onto the star occurs in episodic bursts, which are shorter than accretion outbursts. Hence under certain conditions the star spins down without an outflow, even while some gas leaks onto the stellar surface, loosening the torque-efficiency nexus implied by (C1) and (C2).

A comprehensive treatment of disk trapping involves calculating the radial density profile of the disk near R_c , along the lines developed by D’Angelo & Spruit (2010). Such a calculation does not fit easily into the mathematical framework of the Kalman filter and introduces several new parameters, which would challenge the estimation accuracy of the Kalman filter given current and prospective data volumes. We therefore simplify the treatment using a subset of the analytic scalings formulated by D’Angelo & Spruit (2012). First, we replace the traditional formula (3) for R_m (Ghosh & Lamb 1979) with the following prescription for the inner disk radius, $R_{\text{in}} = R_m - \Delta R$: we solve

$$\frac{Q_{\text{co}}(t)}{Q(t)} = \frac{1}{2} \left\{ 1 - \tanh \left[\frac{R_{\text{in}}(t) - R_c(t)}{\Delta R_2} \right] \right\}. \quad (\text{C5})$$

and

$$R_{\text{in}}(t) = \frac{\Omega(t)Q_{\text{co}}(t)}{\pi S(t)} \quad (\text{C6})$$

simultaneously for $R_{\text{in}}(t)$ and $Q_{\text{co}}(t)$ as functions of $Q(t)$ and $S(t)$, so that we can calculate the radiative efficiency

$$\eta(t) = \frac{Q_{\text{co}}(t)}{Q(t)} \quad (\text{C7})$$

in terms of $Q(t)$ and $S(t)$. Equations (C5) and (C6) resemble (C2); see also equations (19) and (20) in D’Angelo & Spruit (2010). They capture approximately how mass transfer onto the stellar surface ceases in the propeller regime $R_{\text{in}} > R_c$. However there are two subtleties of interpretation: (i) $R_{\text{in}} = R_m - \Delta R$ replaces R_m in the right-hand side of (C5); and (ii) $Q_{\text{co}}(t)$ is the mass accretion rate in the reference frame comoving with $R_{\text{in}}(t)$ at speed $\dot{R}_{\text{in}}(t)$, so we have $Q_{\text{co}}(t) \neq Q(t)$ in general except at magnetocentrifugal equilibrium ($R_{\text{in}} = R_c$). Equation (C6) replaces (3). Physically it describes the balance between the angular momentum flux (equivalently the torque that makes the disk corotate with the star) and the Maxwell stress at R_{in} ; see equation (6) in D’Angelo & Spruit (2010) and also Spruit & Taam (1993). Again there is a subtlety of interpretation: here $S(t)$ is the $z\phi$ -component of the Maxwell stress tensor, which is $\eta_B = B_\phi/B_z$ times the zz -component in (3). Assuming a dipole magnetic field and hence $S(t) = (4\pi)^{-1}\eta_B\mu^2R_{\text{in}}^{-6}$ inside the magnetosphere, where

μ is the star’s magnetic moment, we obtain from (C6) the equivalent formula

$$R_{\text{in}}(t) = \left[\frac{\eta_B \mu^2}{4\Omega(t)Q_{\text{co}}(t)} \right]^{1/5}, \quad (\text{C8})$$

which replaces (8) and agrees with equation (7) in D’Angelo & Spruit (2010). Physically, the above description is consistent with the general observation by Wang (1987), that the growth rate of the toroidal field due to differential rotation is proportional to B_z [rather than B_ϕ as in Ghosh & Lamb (1979)], which also ensures that the magnetic pressure $\sim B_\phi^2/(8\pi)$ in the wound-up field remains lower than the thermal pressure for $r \gtrsim R_c$ and therefore does not disrupt the thin disk.

What is the torque law in the context of disk trapping? As in the traditional picture (Ghosh & Lamb 1979), the torque on the star comprises a spin-up component, transmitted by the gas penetrating the magnetosphere and falling onto the stellar surface, and a spin-down component, which arises from the interaction between the magnetic field and the disk at $r \gtrsim R_c$. The two components are approximated by (D’Angelo & Spruit 2012; Gençali et al. 2022)

$$I \frac{d\Omega}{dt} = Q(t)[GM R_{\text{in}}(t)]^{1/2} - 2\pi S(t) R_{\text{in}}(t)^2 \Delta R \left\{ 1 + \tanh \left[\frac{R_{\text{in}}(t) - R_c(t)}{\Delta R} \right] \right\}, \quad (\text{C9})$$

which is the same as equation (12) in D’Angelo & Spruit (2012) and replaces (5) in the main text. Physically (C9) resembles (5), in the sense that it implies $d\Omega/dt > 0$ for $R_{\text{in}} < R_c$, where the hyperbolic tangent suppresses the magnetic torque, and $d\Omega/dt < 0$ for $R_{\text{in}} > R_c$, where the magnetic torque dominates. However, there are some subtleties. (i) The lever arm of the material component is $R_{\text{in}} = R_m - \Delta R$ rather than R_m . (ii) The width ΔR of the interaction region appears explicitly in the second term on the right-hand side of (C9) to allow for the scenario $\Delta R \ll R_c$, unlike in (5), where the factor $1 - (R_m/R_c)^{3/2}$ implicitly assumes $\Delta R \sim R_c$. (iii) The hyperbolic tangent smoothing function involves ΔR rather than ΔR_2 , because the width of the interaction region is governed by related but different physics to the propeller transition in Appendix C.2. (iv) $S(t) \propto \eta_B \mu^2$ in (C9) is the $z\phi$ -component of the Maxwell stress tensor, cf. the zz -component in (5). (v) Zero torque occurs at $R_{\text{in}} \approx R_c$ but not $R_{\text{in}} = R_c$ exactly, implying $\eta(t) \approx 0.5$ at zero torque.

Figure 6 displays results from a repeat of the numerical experiment in Figures 1–3 with disk trapping incorporated, i.e. with (5) and (11) replaced by (C9) and (C7) respectively, supplemented by (C5) and (C6). Equations (9) and (10) are also replaced by (B1) and (B2) to allow for disequilibrium. The revised model features nine parameters Θ to be estimated. One possible combination is $\Theta = (\beta_6, \beta_7, \beta_8, \beta_9, \beta_{10}, \gamma_Q, \gamma_S, \sigma_{QQ}, \sigma_{SS})$, with

$$\beta_6 = \frac{(GM)^{1/2} \bar{Q}^{3/2}}{\pi^{1/2} I \bar{S}^{1/2} \bar{\Omega}^{1/2}}, \quad (\text{C10})$$

$$\beta_7 = \frac{2\overline{Q}^2\overline{\Omega}\Delta R}{\pi I\overline{S}}, \quad (\text{C11})$$

$$\beta_8 = \frac{\overline{\Omega}\overline{Q}}{\pi\overline{S}\Delta R_2}, \quad (\text{C12})$$

$$\beta_9 = \frac{(GM)^{1/3}}{\overline{\Omega}^{2/3}\Delta R_2}, \quad (\text{C13})$$

and

$$\beta_{10} = \frac{\Delta R}{\Delta R_2}. \quad (\text{C14})$$

We employ an unscented Kalman filter to do the nonlinear analysis (Julier & Uhlmann 1997), as in Appendices B and C.2, with $N = 5 \times 10^2$. We find, as in Appendix C.2, that the Kalman filter tracks $\Omega(t)$ and $\eta(t)$ accurately; the solid, colored and dashed, black curves in the third and fourth panels on the left of Figure 6 overlap closely. The filter also tracks $Q(t)$ and $S(t)$ accurately; the results resemble Figure 4 and are not plotted for brevity. The graph of $\eta(t)$ (fourth panel on the left of Figure 6) shows a smoother version of the episodic accretion seen in Figure 5 in D’Angelo & Spruit (2012). “Dumping” episodes occur during the intervals $0.7 \lesssim t/(10^8 \text{ s}) \lesssim 0.9$ and $1.7 \lesssim t/(10^8 \text{ s}) \lesssim 1.9$, accompanied by spikes in $\eta(t)$. The dumping episodes are less pronounced than in D’Angelo & Spruit (2012), because the more realistic accretion model in D’Angelo & Spruit (2012) lets more gas pile up at the inner edge of the disk. We deliberately choose $\Delta R = 0.85R_{\text{m}0}$ and $\Delta R_2 = 0.65R_{\text{m}0}$ to be higher than suggested by D’Angelo & Spruit (2012), in order to match the $\eta(t)$ behavior qualitatively.¹⁴ The estimation accuracy of the Kalman filter as a function of γ_Q , γ_S , σ_{QQ} , σ_{SS} , and ΔR_2 is studied in §4 and Appendix C.2, so here we focus on ΔR . The right panel of Figure 6 displays the marginalized posterior of ΔR , with the other parameters taken as known artificially to accelerate the computation. We find that the error in the peak and the uncertainty (full width half maximum) are given by ≈ 0.020 dex and ≈ 0.011 dex respectively, including a systematic but negligibly small bias like in Figure 4. A preliminary analysis indicates that $N \geq 2 \times 10^3$ samples are needed to achieve convergence when scanning the complete parameter space, as in Appendix C.2, above what is available typically today.

¹⁴Smaller values of ΔR and ΔR_2 yield episodic accretion, when one solves for the disk surface density profile self-consistently; see §3 and §4 in D’Angelo & Spruit (2010) and §2 in D’Angelo & Spruit (2012). However, it is challenging to incorporate the disk structure into the Kalman filter framework, as discussed above, so we set ΔR and ΔR_2 artificially high to compensate for the purpose of testing. D’Angelo & Spruit (2012) argued that one has $\Delta R_2 \lesssim \Delta R < R_{\text{m}0}$ typically, and that ΔR must exceed a minimum threshold to suppress disruption by the Kelvin-Helmholtz instability.

A full study of the estimation accuracy is postponed, until larger volumes of astronomical data establish the need.

The results in Figure 6 are encouraging. Nonetheless we emphasize that the revised equations of motion are still idealized. Firstly, (C7) ascribes the efficiency $\eta(t)$ entirely to nonconservative mass transfer; the radiative processes modeled phenomenologically through γ_η and $\sigma_{\eta\eta}$ in (11) are missing. Secondly, we cannot track easily the disk density profile within the Kalman filter framework, so we observe gentler episodic dumping of gas onto the stellar surface than in D’Angelo & Spruit (2010), even though we capture the smoother disk trapping dynamics inherent in the torque and mass transfer laws (C5)–(C9). Thirdly, in common with D’Angelo & Spruit (2010), we do not track the evolution of $B_\phi(t)$ and $B_z(t)$ separately, nor do we resolve the system variables spatially in ϕ and z , so we are blind to the rich phenomena observed in three-dimensional magnetohydrodynamic simulations, such as finger-like accretion channels from Rayleigh-Taylor instabilities (Romanova et al. 2003, 2005; Zanni & Ferreira 2013; Romanova & Owocki 2015). Some of the latter physics may be captured crudely by the mean-reverting dynamics in (9) and (10), parametrized by γ_Q , γ_S , σ_{QQ} , and σ_{SS} . It remains to be seen, however, whether white-noise fluctuations are representative of such processes even as a rough approximation, e.g. upon analyzing PSDs from the simulations; see Figures 6 and 11 in Romanova et al. (2021) for example.

C.4. Outflows

Three-dimensional magnetohydrodynamic simulations reveal that the inflow physics in §2 and Appendices C.1–C.3 is supplemented by outflows under a range of conditions; see Romanova & Owocki (2015) for a review. Outflows can be launched by several mechanisms: (i) magnetocentrifugal slingshot along open magnetic field lines anchored in the disk, as long as they are inclined favorably (Blandford & Payne 1982); (ii) episodic ejection of plasmoids, when the magnetic pressure $\sim B_\phi^2/(8\pi)$ inflates the disk and severs temporarily its magnetic connection back to the star, before reconnection restores it (Lai 2014; Uzdensky 2004); (iii) magnetocentrifugal slingshot powered by the corotating magnetosphere in the propeller regime; (iv) field line bunching near R_m , which drives a conical, polar outflow for $R_m < R_c$ (Romanova et al. 2009; Romanova & Owocki 2015); and (v) outward redirection of an accretion flow along open magnetic field lines anchored in the star rather than the disk (Matt & Pudritz 2005, 2008; D’Angelo 2017).

In order to incorporate an outflow into the Kalman filter framework, one needs an equation of motion for the mass ejection rate $Q_w(t)$. This is not easy to write down analytically; $Q_w(t)$ depends on the complicated magnetic topology and thermodynamics at the base of

the outflow, which are not understood fully. One may elect to bundle the complications into a mean-reverting Langevin equation, analogous to (9)–(11), but this raises the number of parameters to be estimated from seven to nine and may not be accurate physically. Alternatively, one may draw upon phenomenological scalings in the literature, e.g. equation (5) in Matt & Pudritz (2005) for $Q_w(t)$, which introduces a new thermodynamic parameter. Likewise, the spin-down torque exerted by a wind of type (v) in the previous paragraph can be estimated phenomenologically as (Matt & Pudritz 2008; D’Angelo 2017)

$$I \left. \frac{d\Omega}{dt} \right|_w \propto -Q_w(t)\Omega(t)R_m(t)^2, \quad (\text{C15})$$

with

$$R_m(t) \propto [Q_w(t)/S(t)]^{m'} \quad (\text{C16})$$

and $m' \approx 0.5$, equivalent to equations (2) and (3) in Matt & Pudritz (2008) with $S \propto \mu^2 R_m^{-6}$. The above scalings raise the number of parameters from seven to 10. Equations (C15) and (C16) have been generalized semianalytically to interpolate between accretor ($R_m < R_c$) and propeller ($R_m > R_c$) regimes (Ireland et al. 2022) and to model advection-dominated super-Eddington systems (Chashkina et al. 2019) and plasmoid ejection (Zanni & Ferreira 2013).

In light of the above challenges and in keeping with the scope of this paper, we postpone the inclusion of outflows in the Kalman filter framework, until larger data sets are available, which justify estimating more parameters.

D. Identifiability analysis

In an arbitrary Kalman filter, the number of measurement variables (here two, namely P and L) does not necessarily equal the number of hidden state variables (here four, namely Ω , Q , S , and η , for the linear model in §2.5) nor the number of system parameters [here seven, namely $\Theta = (\gamma_\Omega, \gamma_A, \sigma_{AA})$ with $A \in \{Q, S, \eta\}$, for the linear model in §2.5]. Several scenarios are therefore possible. Sometimes the system parameters can be inferred uniquely, even when there are fewer measurement variables than hidden state variables. On other occasions the opposite holds: some parameters cannot be inferred uniquely, no matter how plentiful the data are, because they enter through combinations that cannot be disentangled, even when there are more measurement variables than hidden state variables. What scenario applies to any specific problem can be determined by performing a formal *identifiability analysis* on the dynamical and measurement equations of the Kalman filter. An identifiability analysis is a standard tool in electrical engineering (Bellman & Åström 1970). In this appendix

we apply it to the linearized system in §2.5 and find that all seven system parameters $\Theta = (\gamma_\Omega, \gamma_A, \sigma_{AA})$ with $A \in \{Q, S, \eta\}$ can be identified from the measured time series $P(t_n)$ and $L(t_n)$. Identifiability analyses for the generalized, nonlinear models in Appendices B and C are postponed, until data volumes grow to the point where such models are applied in practice.

To test for identifiability, we must count the number of independent constraints imposed on Θ by the data, acting through the Kalman recursion relations in §3.2. We begin the analysis in the absence of noise. Transforming temporarily from discrete to continuous time for the sake of notational convenience, we have $\dot{\mathbf{X}} = \mathbf{A}\mathbf{X}$ and $\mathbf{Y} = \mathbf{C}\mathbf{X}$, with the 4×4 matrix \mathbf{A} and 2×4 matrix \mathbf{C} defined in §3.2. We now seek to write \mathbf{X} in terms of \mathbf{Y} . As the rank of \mathbf{Y} is less than the rank of \mathbf{X} , we must supplement \mathbf{Y} with its derivatives $\dot{\mathbf{Y}}$ and $\ddot{\mathbf{Y}}$. In discrete time, this is equivalent to supplementing $P(t_n)$ and $L(t_n)$ with $P(t_{n-1})$, $L(t_{n-1})$, $P(t_{n-2})$, and $L(t_{n-2})$. In continuous time, we obtain $\dot{\mathbf{Y}} = \mathbf{C}\dot{\mathbf{X}} = \mathbf{C}\mathbf{A}\mathbf{X}$ and $\ddot{\mathbf{Y}} = \mathbf{C}\mathbf{A}^2\mathbf{X}$. Upon combining the expressions for \mathbf{Y} and $\dot{\mathbf{Y}}$ in terms of \mathbf{X} , we obtain four independent, linear equations, viz.

$$\begin{pmatrix} P_1 \\ L_1 \\ \dot{P}_1 \\ \dot{L}_1 \end{pmatrix} = \begin{pmatrix} -1 & 0 & 0 & 0 \\ 0 & 1 & 0 & 1 \\ \gamma_\Omega & \lambda_0 & -\lambda_0 & 0 \\ 0 & -\gamma_Q & 0 & -\gamma_\eta \end{pmatrix} \begin{pmatrix} \Omega_1 \\ Q_1 \\ S_1 \\ \eta_1 \end{pmatrix}, \quad (\text{D1})$$

with $\lambda_0 = 3\gamma_\Omega/5$. The 4×4 matrix on the right-hand side of (D1) is invertible for $\gamma_Q \neq \gamma_\eta$, whereupon we can solve for Ω_1 , Q_1 , S_1 , and η_1 in terms of P_1 , L_1 , \dot{P}_1 , and \dot{L}_1 or, in discrete terms, $P_1(t_n)$, $L_1(t_n)$, $P_1(t_{n-1})$, and $L_1(t_{n-1})$. That is, all four hidden state variables can be recovered as functions of time from the measured time series.

To check which of the system parameters Θ are identifiable, we evaluate $\ddot{\mathbf{Y}} = \mathbf{C}\mathbf{A}^2\mathbf{X}$. The matrix algebra is straightforward and yields

$$\begin{pmatrix} \ddot{P}_1 \\ \ddot{L}_1 \end{pmatrix} = \begin{pmatrix} -\gamma_\Omega^2 & -\lambda_0(\gamma_\Omega + \gamma_Q) & \lambda_0(\gamma_\Omega + \gamma_S) & 0 \\ 0 & \gamma_Q^2 & 0 & \gamma_\eta^2 \end{pmatrix} \begin{pmatrix} \Omega_1 \\ Q_1 \\ S_1 \\ \eta_1 \end{pmatrix}. \quad (\text{D2})$$

Rewriting the hidden state variables in terms of P_1 , L_1 , \dot{P}_1 , and \dot{L}_1 with the aid of (D1), we arrive at

$$\begin{pmatrix} \ddot{P}_1 \\ \ddot{L}_1 \end{pmatrix} = \begin{pmatrix} -\gamma_S\gamma_\Omega & \frac{\lambda_0\gamma_\eta(\gamma_Q - \gamma_S)}{\gamma_Q - \gamma_\eta} & -(\gamma_\Omega + \gamma_S) & \frac{\lambda_0(\gamma_Q - \gamma_S)}{\gamma_Q - \gamma_\eta} \\ 0 & -\gamma_\eta\gamma_Q & 0 & -(\gamma_Q + \gamma_\eta) \end{pmatrix} \begin{pmatrix} P_1 \\ L_1 \\ \dot{P}_1 \\ \dot{L}_1 \end{pmatrix}. \quad (\text{D3})$$

Equation (D3) is a system of ordinary differential equations involving measurement variables and their derivatives only, namely P_1 , L_1 , \dot{P}_1 , \dot{L}_1 , \ddot{P}_1 , and \ddot{L}_1 . Hence all six nonzero elements of the 2×4 matrix on the right-hand side can be estimated (“identified”) with enough data. It is easy to resolve the six measured elements into γ_Q , γ_S , and γ_η , along with γ_Ω (which involves equilibrium quantities only).

The above analysis is performed on the noise-free Kalman equations. It does not guarantee that the noise amplitudes σ_{QQ} , σ_{SS} , and $\sigma_{\eta\eta}$ are identifiable. Experience across many electrical engineering applications suggests that noise amplitudes are usually identifiable (Bellman & Åström 1970), because they are transformed versions of the dispersions of the measurement variables, e.g. $\langle [P(t_n) - \langle P(t_n) \rangle]^2 \rangle^{1/2}$. To check this formally for the system in §2.5, we calculate the covariance matrices \mathbf{V} and \mathbf{W} of the hidden state and measurement variables respectively, with components $V_{ij} = \langle \delta X_i(t) \delta X_j(t) \rangle$, $W_{ij} = \langle \delta Y_i(t) \delta Y_j(t) \rangle$, $\delta X_i(t) = X_i(t) - \langle X_i(t) \rangle$, and $\delta Y_i(t) = Y_i(t) - \langle Y_i(t) \rangle$, assuming nonzero process noise but zero measurement noise. We then count the number of independent parameters in \mathbf{V} and compare with the number of independent pieces of measured information in \mathbf{W} .

The covariance matrices are defined as usual by (Gardiner 1994)

$$\mathbf{V} = \int_0^t dt' \exp(\mathbf{A}t') \mathbf{\Sigma} \exp(\mathbf{A}^\top t') \quad (\text{D4})$$

and

$$\mathbf{W} = \mathbf{C} \mathbf{V} \mathbf{C}^\top, \quad (\text{D5})$$

with $\mathbf{\Sigma} = \text{diag}(0, \sigma_{QQ}^2/Q_0^2, \sigma_{SS}^2/S_0^2, \sigma_{\eta\eta}^2/\eta_0^2)$ for the special case of uncorrelated white noise in (12). The superscript T denotes the matrix transpose. Recall that Q_0 , S_0 , and η_0 are expressible in terms of γ_Ω through (A4)–(A6). It is straightforward to evaluate (D4) and (D5) for the 4×4 matrix \mathbf{A} and 2×4 matrix \mathbf{C} defined in §3.2. We write down the nonzero,

independent components for reference as follows:

$$V_{\Omega\Omega} = \frac{\lambda_0^2 \sigma_{QQ}^2}{2Q_0^2} \left[-\frac{(-1 + e^{-2\gamma\Omega t})}{\gamma\Omega(\gamma\Omega - \gamma_Q)^2} - \frac{(-1 + e^{-2\gamma_Q t})}{\gamma_Q(\gamma\Omega - \gamma_Q)^2} - \frac{4(1 - e^{-\gamma\Omega t - \gamma_Q t})}{(\gamma\Omega + \gamma_Q)(\gamma\Omega - \gamma_Q)^2} \right] + \frac{\lambda_0^2 \sigma_{SS}^2}{2S_0^2} \left[-\frac{(-1 + e^{-2\gamma\Omega t})}{\gamma\Omega(\gamma\Omega - \gamma_S)^2} - \frac{(-1 + e^{-2\gamma_S t})}{\gamma_S(\gamma\Omega - \gamma_S)^2} - \frac{4(1 - e^{-\gamma\Omega t - \gamma_S t})}{(\gamma\Omega + \gamma_S)(\gamma\Omega - \gamma_S)^2} \right], \quad (\text{D6})$$

$$V_{\Omega Q} = \frac{\lambda_0 \sigma_{QQ}^2}{2(\gamma\Omega - \gamma_Q)Q_0^2} \left[\frac{-1 + e^{-2\gamma_Q t}}{\gamma_Q} + \frac{2(1 - e^{-\gamma\Omega t - \gamma_Q t})}{\gamma\Omega + \gamma_Q} \right], \quad (\text{D7})$$

$$V_{\Omega S} = \frac{\lambda_0 \sigma_{SS}^2}{2(\gamma\Omega - \gamma_S)S_0^2} \left[\frac{1 - e^{-2\gamma_S t}}{\gamma_S} + \frac{2(-1 + e^{-\gamma\Omega t - \gamma_S t})}{\gamma\Omega + \gamma_S} \right], \quad (\text{D8})$$

$$V_{QQ} = \frac{(1 - e^{-2\gamma_Q t})\sigma_{QQ}^2}{2\gamma_Q Q_0^2}, \quad (\text{D9})$$

$$V_{SS} = \frac{(1 - e^{-2\gamma_S t})\sigma_{SS}^2}{2\gamma_S S_0^2}, \quad (\text{D10})$$

$$V_{\eta\eta} = \frac{(1 - e^{-2\gamma_\eta t})\sigma_{\eta\eta}^2}{2\gamma_\eta \eta_0^2}, \quad (\text{D11})$$

and

$$W_{PP} = V_{\Omega\Omega}, \quad (\text{D12})$$

$$W_{PL} = -V_{\Omega Q}, \quad (\text{D13})$$

$$W_{LL} = V_{QQ} + V_{\eta\eta}. \quad (\text{D14})$$

Upon combining (D6)–(D14), we arrive at the set of linear equations

$$\begin{pmatrix} W_{PP} \\ W_{PL} \\ W_{LL} \end{pmatrix} = \begin{pmatrix} M_{11} & M_{12} & 0 \\ M_{21} & 0 & 0 \\ M_{31} & 0 & M_{33} \end{pmatrix} \begin{pmatrix} \sigma_{QQ}^2/Q_0^2 \\ \sigma_{SS}^2/S_0^2 \\ \sigma_{\eta\eta}^2/\eta_0^2 \end{pmatrix}, \quad (\text{D15})$$

with

$$M_{11} = \frac{\lambda_0^2}{2} \left[-\frac{-1 + e^{-2\gamma\Omega t}}{\gamma\Omega(\gamma\Omega - \gamma_Q)^2} - \frac{-1 + e^{-2\gamma_Q t}}{\gamma_Q(\gamma\Omega - \gamma_Q)^2} - \frac{4(1 - e^{-\gamma\Omega t - \gamma_Q t})}{(\gamma\Omega + \gamma_Q)(\gamma\Omega - \gamma_Q)^2} \right], \quad (\text{D16})$$

$$M_{12} = \frac{\lambda_0^2}{2} \left[-\frac{-1 + e^{-2\gamma\Omega t}}{\gamma\Omega(\gamma\Omega - \gamma_S)^2} - \frac{-1 + e^{-2\gamma_S t}}{\gamma_S(\gamma\Omega - \gamma_S)^2} - \frac{4(1 - e^{-\gamma\Omega t - \gamma_S t})}{(\gamma\Omega + \gamma_S)(\gamma\Omega - \gamma_S)^2} \right], \quad (\text{D17})$$

$$M_{21} = -\frac{\lambda_0}{2(\gamma\Omega - \gamma_Q)} \left[\frac{-1 + e^{-2\gamma_Q t}}{\gamma_Q} + \frac{2(1 - e^{-\gamma\Omega t - \gamma_Q t})}{\gamma\Omega + \gamma_Q} \right], \quad (\text{D18})$$

$$M_{31} = \frac{1 - e^{-2\gamma_Q t}}{2\gamma_Q}, \quad (\text{D19})$$

$$M_{33} = \frac{1 - e^{-2\gamma_\eta t}}{2\gamma_\eta}. \quad (\text{D20})$$

The 3×3 matrix in (D15) is invertible, so the noise amplitudes can be solved in terms of the data in \mathbf{W} , together with γ_Q , γ_S , γ_η , and γ_Ω from (D3), and the equilibrium state. That is, σ_{QQ} , σ_{SS} , and $\sigma_{\eta\eta}$ are identifiable in principle.

Ultimately identifiability must be verified empirically for a finite data set. The results in §4 imply that the parameters $\Theta = (\gamma_\Omega, \gamma_A, \sigma_{AA})$ with $A \in \{Q, S, \eta\}$ are identifiable in practice for typical data volumes in the application studied in this paper.

As an aside of physical interest, equations (D6)–(D11) imply that the spin fluctuations Ω_1 are much smaller in magnitude than the fluctuations Q_1 , S_1 , and η_1 of the hidden state variables, as seen in Figure 1 and discussed in §4.2. A typical accretion-powered pulsar has $\gamma_\Omega \ll \gamma_A$ with $A \in \{Q, S, \eta\}$. Physically, torque fluctuations of a given fractional amplitude drive spin fluctuations of a smaller fractional amplitude, because the star’s moment of inertia is large. Evaluating (D6)–(D11) in the regime $\gamma_\Omega \ll \gamma_A$, we obtain the leading-order scalings $V_{\Omega\Omega} \sim (\gamma_\Omega/\gamma_Q^2)(\sigma_{QQ}^2/Q_0^2) + (\gamma_\Omega/\gamma_S^2)(\sigma_{SS}^2/S_0^2)$, $V_{QQ} \sim \sigma_{QQ}^2/(\gamma_Q Q_0^2)$, $V_{SS} \sim \sigma_{SS}^2/(\gamma_S S_0^2)$, and $V_{\eta\eta} \sim \sigma_{\eta\eta}^2/(\gamma_\eta \eta_0^2)$. The scalings imply $V_{\Omega\Omega}/V_{QQ} \sim \max[\gamma_\Omega/\gamma_Q, (\gamma_\Omega/\gamma_S)(\gamma_Q/\gamma_S)(\sigma_{SS}^2/S_0^2)(\sigma_{QQ}^2/Q_0^2)^{-1}] \ll 1$, consistent with Figure 1; the variances $V_{\Omega\Omega}$ and V_{QQ} measure the characteristic magnitudes of the fluctuations Ω_1 and Q_1 respectively. A similar conclusion follows for $V_{\Omega\Omega}/V_{SS}$ and $V_{\Omega\Omega}/V_{\eta\eta}$.

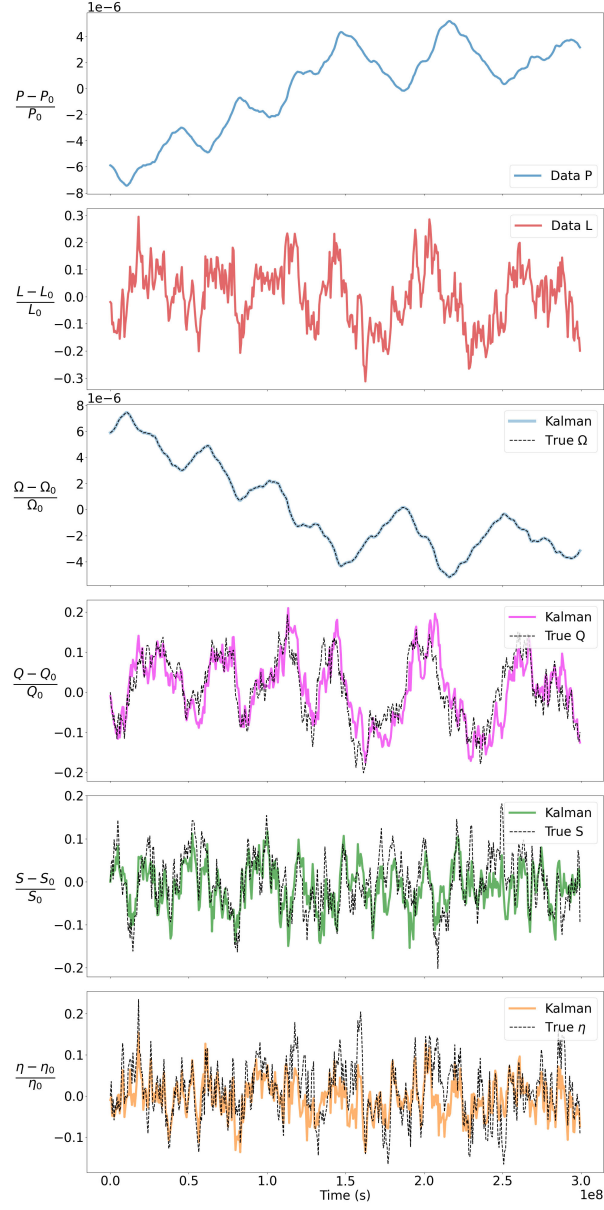


Fig. 1.— Kalman state tracking applied to the hypothetical accretion-powered pulsar with the parameters in Table 1. Inputs: synthetic measurements of spin fluctuations $P_1(t_n)$ (top panel) and X-ray luminosity fluctuations $L_1(t_n)$ (second panel) versus time t_n (units: s), with $0 < t_1 \leq \dots \leq t_{500} = 3.0 \times 10^8$ s. Outputs: state variables $\Omega_1(t_n)$ (third panel), $Q_1(t_n)$ (fourth panel), $S_1(t_n)$ (fifth panel), and $\eta_1(t_n)$ (bottom panel) versus time t_n (units: s). In the bottom four panels, colored, solid curves indicate the squared-error-minimizing, reconstructed state sequence $\hat{\mathbf{X}}(t_n)$ generated by the Kalman filter, and black, dashed curves indicate the true, injected state sequence $\mathbf{X}(t_n)$. The vertical axis in every panel displays a fractional and therefore dimensionless quantity.

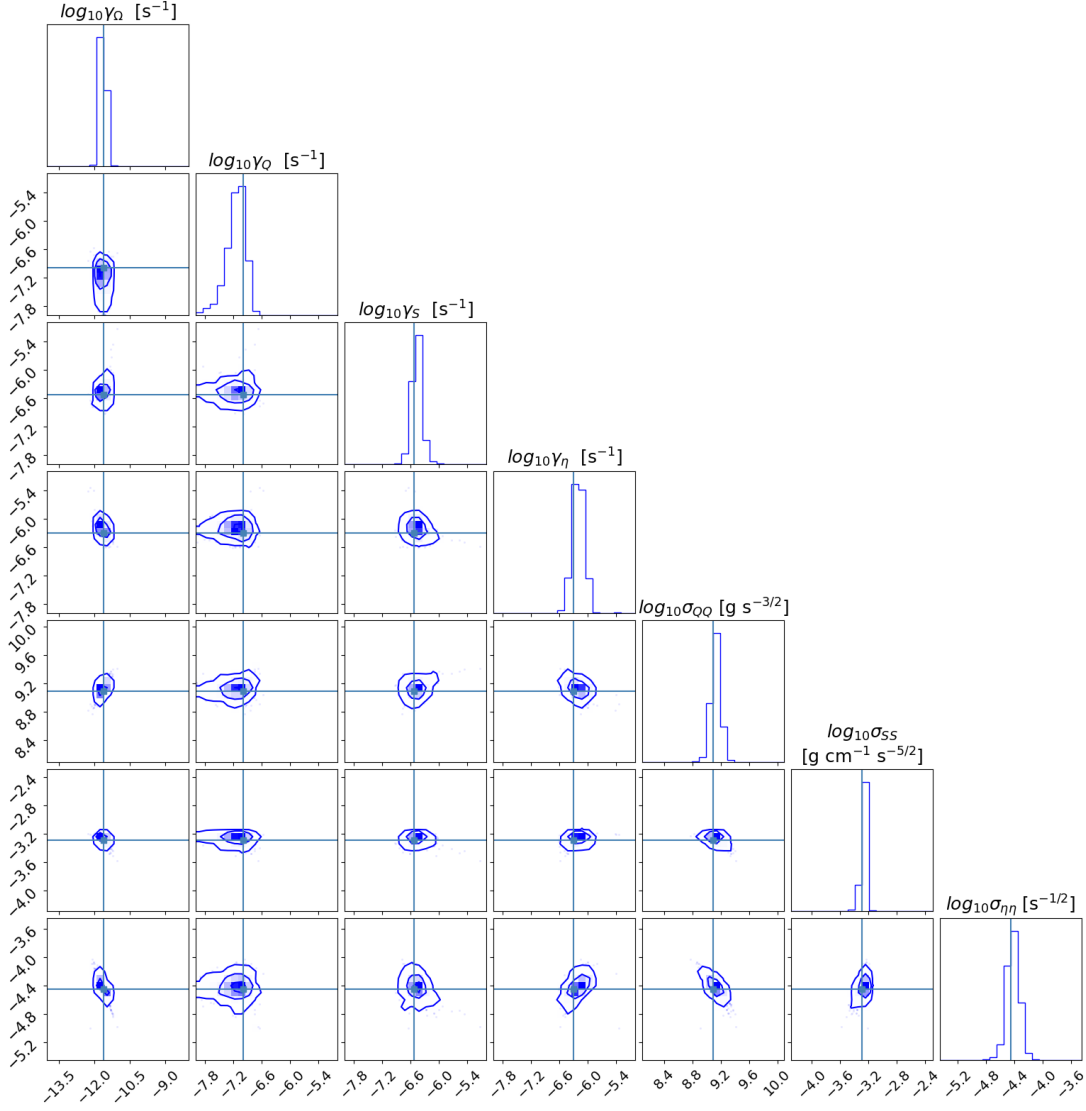


Fig. 2.— Corner plot of the posterior distribution of the model parameters Θ for the hypothetical accretion-powered pulsar in Table 1, viz. γ_Ω , γ_Q , γ_S , γ_η , σ_{QQ} , σ_{SS} , and $\sigma_{\eta\eta}$ (left to right and top to bottom). All quantities are plotted on a log scale (base 10). Contour plots depict the posterior distribution marginalized over five out of seven parameters, e.g. the bottom left corner displays the marginalized posterior in the γ_Ω - $\sigma_{\eta\eta}$ plane. Histograms depict the posterior marginalized over six out of seven parameters. The injected parameter values are marked by horizontal and vertical blue lines. The blue lines coincide approximately with the modes of the marginalized posteriors in every panel, implying that the parameters are estimated accurately.

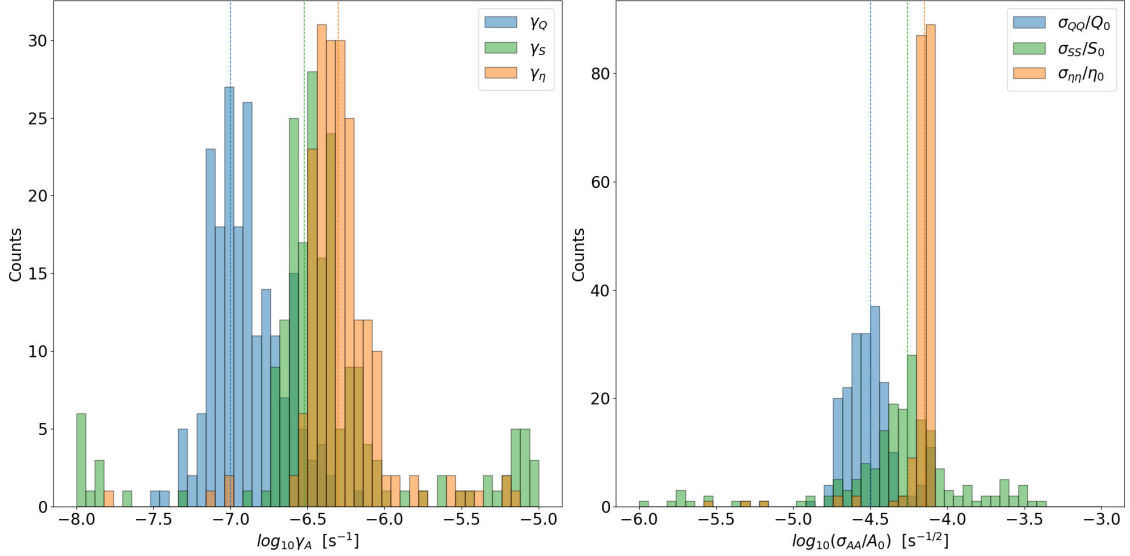


Fig. 3.— Accuracy of parameter estimation with the Kalman filter and nested sampler for the hypothetical accretion-powered pulsar in Table 1. (Left panel.) Histograms of estimated γ_A values (units: s⁻¹), with $A = Q$ (blue), S (green), and η (orange), recovered from 200 random realizations of the synthetic data $P(t_n)$ and $L(t_n)$. The dashed, color-coded, vertical lines correspond to the injected γ_A values in Table 1. All 3×200 estimates fall within the plotted domain. (Right panel.) Histograms of estimated σ_{AA} values, normalized by the equilibrium value A_0 for ease of display, with $A = Q$ (blue; units of s^{-1/2}), S (green; units of s^{-1/2}), and η (orange; units of s^{-1/2}). The dashed, color-coded, vertical lines correspond to the injected values. All estimates fall within the plotted domain, except for 13 σ_{SS} and five $\sigma_{\eta\eta}$ outliers, whose logarithms satisfy $-8 \leq \log_{10}(\sigma_{AA}/A_0) \leq -6$.

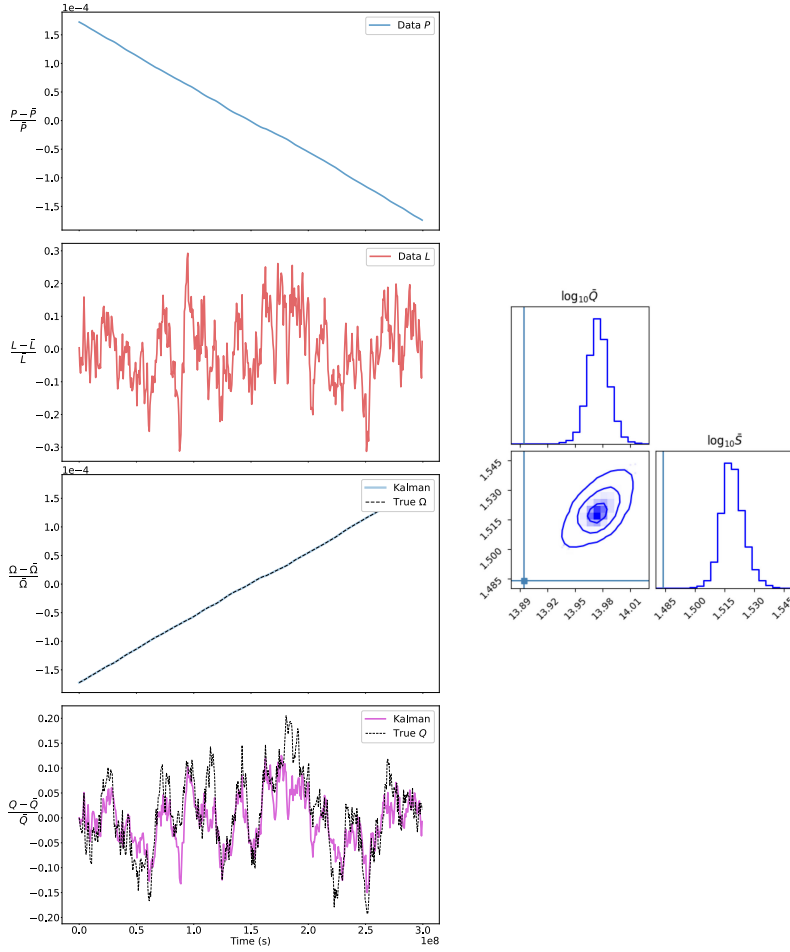


Fig. 4.— Kalman state tracking applied to a hypothetical accretion-powered pulsar in disequilibrium with the parameters in Table 1 except for $\bar{Q} = 2Q_0$ and $\bar{S} = 2^{12/7}S_0$, i.e. spinning up. Inputs: synthetic measurements of spin period $P(t_n)$ (top panel at left) and X-ray luminosity $L(t_n)$ (second panel at left) versus time t_n (units: s), with $0 < t_1 \leq \dots \leq t_{500} = 3.0 \times 10^8$ s. Outputs: state variables $\Omega(t_n)$ (third panel at left) and $Q(t_n)$ (fourth panel at left) versus time t_n (units: s); the other state variables $S(t_n)$ and $\eta(t_n)$ are omitted for clarity, as they resemble Figure 1. Parameter estimation: posterior of \bar{Q} and \bar{S} , marginalized over (γ_A, σ_{AA}) with $A \in \{Q, S, \eta\}$ and presented as a traditional corner plot (contour plot and histograms; panels at right). The injected values are marked by blue horizontal and vertical lines. In the third and fourth panels at left, colored, solid curves indicate the squared-error-minimizing, reconstructed state sequence $\hat{\mathbf{X}}(t_n)$ generated by the Kalman filter, and black, dashed curves indicate the true, injected state sequence $\mathbf{X}(t_n)$. The vertical axes in the four panels at left display fractional and therefore dimensionless quantities.

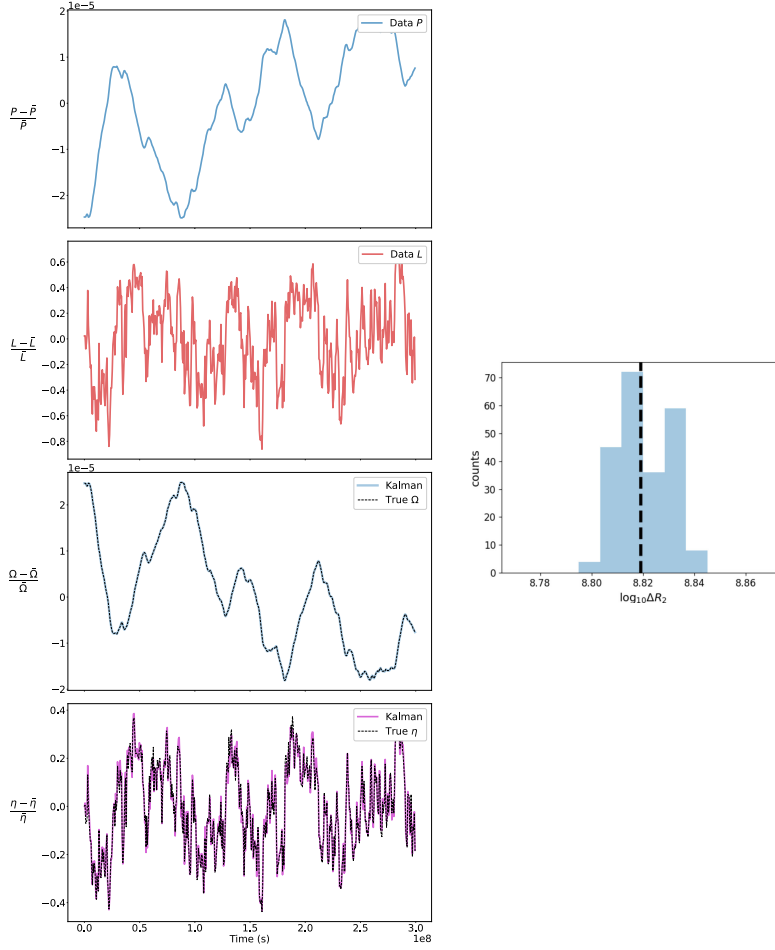


Fig. 5.— Kalman state tracking applied to a hypothetical accretion-powered pulsar with a propeller transition modeled by (C1) and (C2) with $\Delta R_2 = 0.09 R_{m0}$. Inputs: synthetic measurements of spin period $P(t_n)$ (top panel at left) and X-ray luminosity $L(t_n)$ (second panel at left) versus time t_n (units: s), with $0 < t_1 \leq \dots \leq t_{500} = 3.0 \times 10^8$ s. Outputs: state variables $\Omega(t_n)$ (third panel at left) and $\eta(t_n)$ (fourth panel at left) versus time t_n (units: s); the other state variables $Q(t_n)$ and $S(t_n)$ are omitted for clarity, as they resemble Figure 1. Parameter estimation: posterior of ΔR_2 (histogram; panel at right), marginalized over the other six variables in Θ ; the injected value is indicated by the black, dashed, vertical line. For the limited purpose of this test, γ_A and σ_{AA} with $A \in \{Q, S\}$ are assumed known to accelerate the computation but they would be estimated in general as in §4 and Appendix B. In the third and fourth panels at left, colored, solid curves indicate the squared-error-minimizing, reconstructed state sequence $\hat{\mathbf{X}}(t_n)$ generated by the Kalman filter, and black, dashed curves indicate the true, injected state sequence $\mathbf{X}(t_n)$. The vertical axes in the four panels at left display fractional and therefore dimensionless quantities.

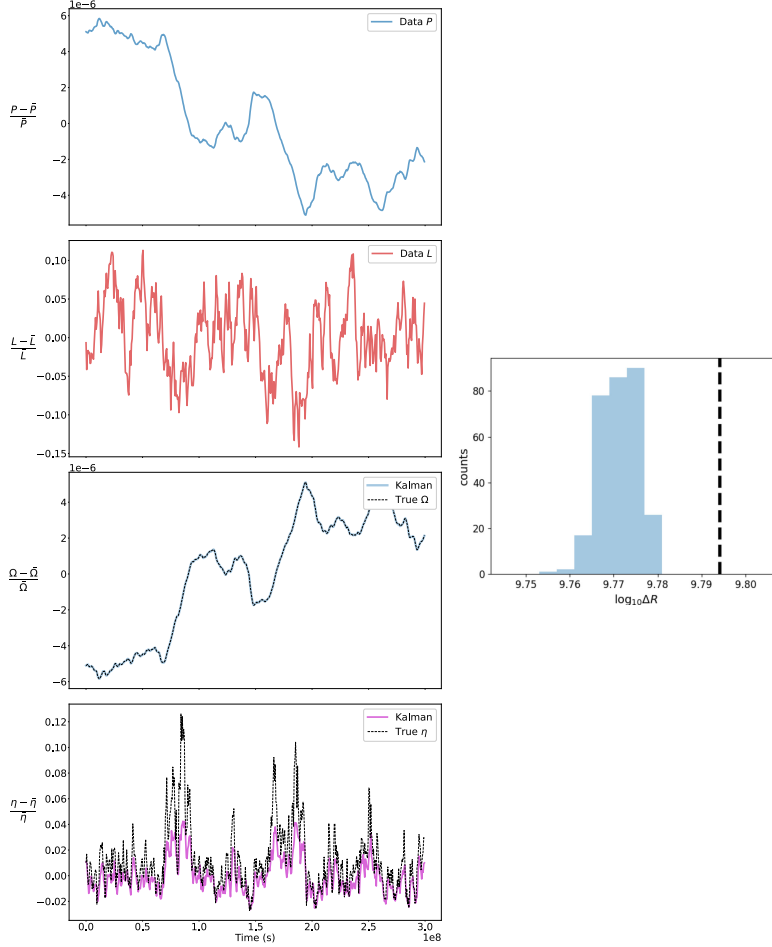


Fig. 6.— As for Figure 5, but incorporating disk trapping modeled by (C5)–(C9) instead of (C1) and (C2), with $\Delta R = 0.80R_{m0}$ and $\Delta R_2 = 0.65R_{m0}$. The axes of the four left-hand panels are the same as in Figure 5. The histogram in the right-hand panel displays the marginalized posterior of ΔR ; the injected value is indicated by the black, dashed, vertical line.